Appendix 3
Pielikums 3

National Research Programme

„Cyber-physical systems, ontologies and biophotonics for safe&smart city and society"

(SOPHIS)

Project No.3

"Biophotonics: imaging, diagnostics and monitoring"

(BF)

Scientific report

Period 1 & 2

2016

Contents

Glossary and abbreviations

IAPS - Institute of Atomic physics and Spectroscopy

RGB - Red-Green-Blue color model

CMOS - Complementary metal-oxide-semiconductor

LED - Light-emitting diode

NIR - Near-infrared spectral band

PPGI - Photoplethysmography imaging technique

FLIR - Forward looking infrared camera

PWTT - Pulse wave transit time

Chapter 3.1

Introduction

Project "Biophotonics: imaging, diagnostics and monitoring" (BF) relates to development of innovative imaging, image processing and biophotonic technologies. The main attention is paid to the following tasks.

1. To develop and experimentally validate new technologies for imaging and image processing, including those for biometry and quantitave assessment of the tissue condition.

   New imaging methods and devices based on principles of photonics - one of the Key Enabling Technologies identified by EU - will be developed and validated. The imaged targets will be living tissues or other bio-objects. This task will be completed in synergy with the 1st project (development of imaging and image processing methods for smart transportation systems) and with the 4th project (video-image processing for recognition of predefined city safety events).

   A novel technology for obtaining several spectral images from a single RGB image data set will be developed. The research will make possible to create an efficient embedded multimodal biometry system with improved safety and simplified image capture.

2. To create innovative biophotonic technologies for non-invasive (including non-contact) clinical diagnostics and monitoring, to develop new concepts, methods and algorithms for implementation in experimental prototype devices and to validate them clinically.

   Bio-object image processing will be developed and integrated for exact applications in clinical diagnostics, e.g. by elaboration of functioning prototype devices for optical diagnostics and monitoring. The developed prototypes and software will be validated in laboratory and clinical environment.

   Innovative solutions will be developed in order to extend the video-imaging technology for remote cardiovascular monitoring into the infrared range of spectrum. Infrared technologies for quantitave assessment of the tissue condition will be developed, as well. The most significant from clinical point will be the newly created and improved image-based optical diagnostic technologies that will essentially speed-up and improve the diagnostic

procedures in dermatology, anaesthesiology, cardiology and other areas of healthcare.

The following document contains detailed description of these research activities in each of the four groups:

- A section 3.2 describes a methodology for obtaining several monochromatic spectral images from the digital color image with further conversion into distribution maps of skin tissue compounds - skin chromophores;
- A section 3.3 describes methodology for non-contact monitoring of cardiovascular parameters by means of infrared illumination and video camera, with applications in regional anesthesia monitoring;
- A section 3.4 describes methodology for assessment of skin moisture by means of infrared imaging, which is applicable to skin moisture estimation for measuring the effect of different moisturizing creams on skin, as well as for medical purposes.
- A section 3.5 describes the technical improvements of previously developed multi-modal imaging prototype device, which is intended for non-contact assessment of skin malformations (melanoma, vascular formations etc.).

Chapter 3.2

Methodology for obtaining several monochromatic spectral images from the data of a single digital color image

3.2.1 Introduction

Distribution maps of tissue compounds, e.g. skin chromophores, provide diagnostic information about the tissue condition and its changes during physiological processes like inflammations, post-therapy recovery, burn healing, development of tumours and bruises, etc. Three main chromophores that determine skin colour in normal conditions are melanin, oxy-haemoglobin and deoxy-haemoglobin. Content of another skin chromophore – bilirubin increases in result of liver insufficiency and/or mechanical interventions (bruises, post-surgery healing; as a reference, see). Fast and reliable 2D-mapping of the named chromophores in pathologic cases is of interest for dermatologists, oncologists, forensic experts, intensive care physicians, family doctors and other professionals, as well as for wider audience interested in self-monitoring, e-medicine, personalized healthcare and similar aspects.

Tissue chromophore maps can be derived from large data sets of multispectral and/or hyperspectral reflection images, by means of spectral fitting algorithms with respect to absorption properties of the chromophores under interest. To avoid errors due to detection of tissue specular reflection, such systems usually comprise two mutually crossed polarizers – one in front of the illuminator and the other in front of the imaging camera. Digital RGB cameras are also well-suited for chromophore mapping, since the red (R), green (G) and blue (B) spectral images of the target can be separated and/or specifically related.

The main principle of this technology is lighting of the object (skin) with the laser light by three or more lasers with different spectral bands. Reflected image can be detected by color (Red-Green-Blue) CMOS image sensor. The captured single-shot image contains three RGB image components, which are

partially mixed due to cross-talk overlap among the RGB sensor channels. First, the RGB crosstalk correction algorithm is needed to getting "clear " spectral images. Then the chromophore maps can be derived from reflected images, by means of spectral fitting algorithms with respect to absorption properties of the chromophores.

Possibility to extract three monochromatic spectral images from a single digital RGB image with further conversion into distribution maps of three main skin chromophores was demonstrated both experimentally and clinically [1][2][3][4][5][6]. This technique considerably speeds-up, simplifies and improves accuracy of the procedure of chromophore mapping in dermatology, oncology, microscopy, artwork expertise and other related areas.

In this work the following tasks were done:

- RGB cross-talk algorithm for three chromatic laser illumination was developed;
- The mathematical model of mapping of skin chromophores was developed;
- Two prototype devices for obtaining three spectral images illuminated by three chromatic laser light were developed;
- The mathematical model was validated on the images of pigmented and vascular skin malformations.

3.2.2 The prototype devices

3.2.2.1 The prototype device for obtaining three spectral images illuminated by laser light at three spectral bands

As the first step, illumination of the object simultaneously by 3 spectral lines with subsequent extraction of 3 monochromatic spectral images from the digital RGB image cube was studied in laboratory. Our experimental setup scheme is presented at Fig.3.2.1. Three lasers with emission wavelengths 473 nm, 532 nm and 659 nm were used for illumination. The output beam of each laser was coupled into a SMA-integrated 7-fiber bundle; outputs of the fibers were joined in a specially made polished metallic ring with randomly distributed distal ends of 21 optical fiber. A diffuser providing uniform illumination of the object plane was placed in front of this light-emitting ring. A conical shielding wall ensured fixed distance between the CMOS camera (placed in center of the emitting ring) and object. The captured image was forwarded to computer and processed by means of the Matlab software.

To suppress the object (e.g. skin) surface-reflected light, two cross-oriented polarizers were used. The first, ring-shaped polarizer was placed after the emitter ring with diffuser; the second polarizer was placed in front of the camera objective. Specifications of the used components are as follows: 659 nm laser - mod. DB650-12-3, 12mW; 532 nm laser - mod. DD532-10-5, 10mW; 473 nm laser - mod. 1011750, 30mW (was attenuated); CMOS image sensor UI-1221LE-C-HQ, 1/3', 752x480 pixels, RGB sensitivities given at Fig.3.2.2.

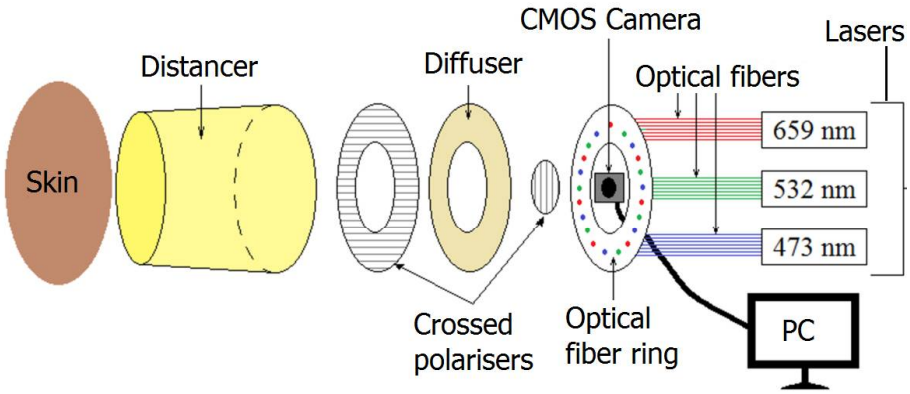

Figure 3.2.1: The experimental setup scheme

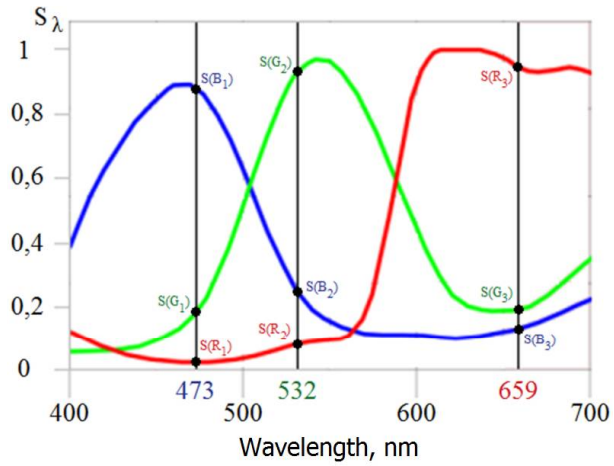

Figure 3.2.2: Spectral sensitivities of the RGB image sensor color channels

3.2.2.2 The prototype device for obtaining three spectral images illuminated by R-G-B laser light

An improved portable three laser line illumination prototype device was designed, assembled and experimentally/clinically tested during the next period. Its design scheme is presented at Fig.3.2.3. Three pairs of identical laser modules (448 nm, 532 nm, 659 nm) were exploited; lasers of each pair were mounted at opposite sides of the inner wall of holding cylinder 8. The six laser beams by means of the collector 14 were directed radially to the ring-shaped diffuser 13 which served as a three laser line source for illumination the object plane. In order to optimize the uniformity of illumination, collectors of laser beams 14 with three different external diameters of the comprised diffuser 13 (30 mm, 40 mm and 50 mm) were fabricated and tested in all possible emission-detection combinations, using a white paper sheet as a target.

Some results are illustrated on Fig.3.2.4; the measurements confirmed that the 50mm external diameter of the diffuser provided the most uniform illumination, so it was selected for use in the further clinical measurements.

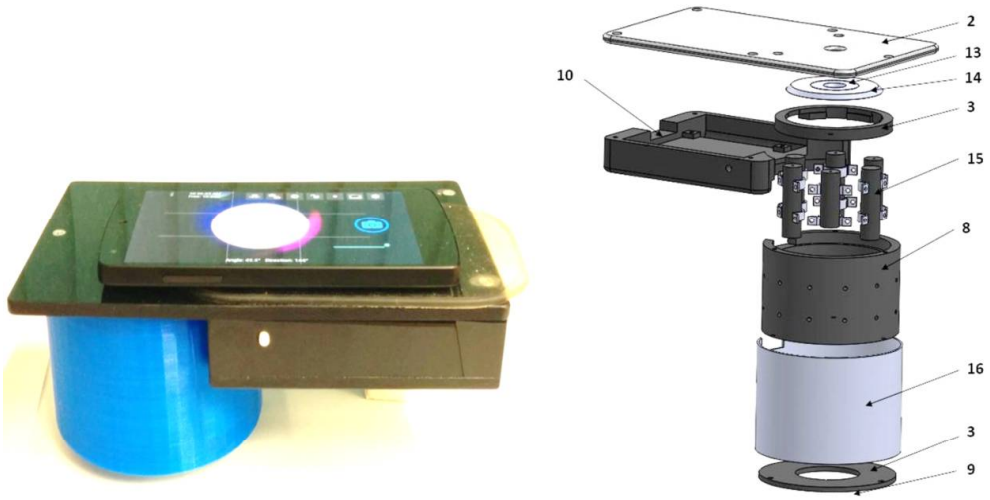

Figure 3.2.3: The portable three laser line illuminator (left) and its design scheme (right)

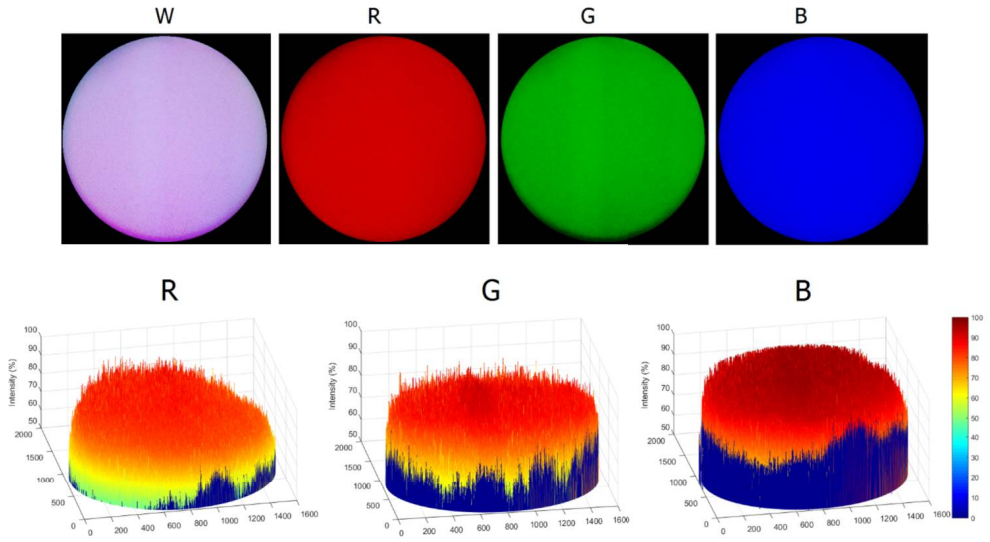

Figure 3.2.4: Uniformity of the object plane illumination: top - simultaneously by all three laser lines (W) and as detected by the three color channels of the image sensor (R, G, B); bottom – illumination intensity distributions if each laser line (R-red, G-green, B-blue) is emitted separately and detected at the corresponding color channel

3.2.3 Algorithms

3.2.3.1 Algorithm for obtaining chromophore maps from RGB color image

Human in-vivo skin was chosen as a bio-tissue target. Distribution maps of the main skin chromophores - melanin, oxy-haemoglobin and deoxy-haemoglobin

were constructed from the single-snapshot RGB image data by using the Lambert-Beer law at each exploited wavelength:

$$\begin{aligned} I_1 &= I_{01} \cdot exp[-(k_{a1} + k_{b1} + k_{c1}) \cdot l_1], \\ I_2 &= I_{02} \cdot exp[-(k_{a2} + k_{b2} + k_{c2}) \cdot l_2], \\ I_3 &= I_{03} \cdot exp[-(k_{a3} + k_{b3} + k_{c3}) \cdot l_3], \end{aligned} \tag{3.2.1}$$

Where I_i - skin reflected intensity at the wavelength λ_i, I_{0i} - reference-reflected intensity at the wavelength λ_i, l_i - mean photon pass-length in the tissue at the wavelength λ_i, k_{ai}, k_{bi} and k_{ci} - absorption coefficients of the three skin chromophores (a - oxy-haemoglobin, b - deoxy-haemoglobin, c - melanin) at the wavelength λ_i (λ_1=473 nm, λ_2=532 nm, λ_3=659 nm).

The absorption coefficients (k_{a1}, k_{b1} and k_{c1}) at wavelength λ_1 can be expressed as:

$$\begin{aligned} k_{a1} &= c_a \cdot \varepsilon_a(\lambda), \\ k_{b1} &= c_b \cdot \varepsilon_b(\lambda), \\ k_{c1} &= c_c \cdot \varepsilon_c(\lambda), \end{aligned} \tag{3.2.2}$$

where c_a, c_b and c_c are the chromophore concentrations and ε_a, ε_b and ε_c - extinction coefficients that are tabulated at each of the exploited wavelengths.

Equations 3.2.1 and 3.2.2 were used to express analytically the values of three chromophore relative concentrations at each image pixel as functions of the measured signals, with subsequent building of three chromophore distribution maps.

3.2.3.2 Algorithm for obtaining of chromophore maps from RGB color image at multi-spectral laser light

The proposed technology for snapshot skin chromophore mapping was further developed by analysis of options to exploit monochromatic spectral images for mapping of a larger number of skin chomophores ($n > 3$). It is generally possible by corresponding increase of the number of spectral lines used for illumination.

The absorption coefficient k_j is expressed as the sum of all skin chromophore concentrations multiplied by the extinction coefficients:

$$k_j = \sum_{i=1}^{n} c_i \cdot \varepsilon_{i,j}, \tag{3.2.3}$$

where $j = 1, 2, \ldots s$ - the number of spectral lines, n is total amount of chromophore types, c_i is the concentration of corresponding chromophore, $\varepsilon_{i,j}$ - extinction coefficients, which are tabulated for each type of chromophore (Table3.2.1).

Distribution maps of the n skin chromophores can be constructed from the snapshot RGB image data by using the Lambert-Beer law at each exploited wavelength:

$$I_j = I_{0j} \cdot exp(-l_j \cdot k_j), \tag{3.2.4}$$

where I_j is reflected light intensity at wavelength λ_j, I_{0j} is the reference intensity; l_j is mean free optical path for skin tissue, which is wavelength dependable; k_j is absorption coefficient.

The photon path length in the skin before returning to the air was chosen as $4l_j$, where l_j is mean penetration depth at λ_j. At λ=473 nm the value of l_j is comparable with the thickness of epidermis; in this case we assumed that the light is absorbed by epidermal melanin (the optical path $=4l_{473}$) and slightly by the dermis hemoglobin (optical path taken twice less - $2l$). At 532 nm and 659 nm, melanin absorption path in the epidermis was approximated at $4l_{473}$, hemoglobin absorption path in dermis respectively is $4(l_{532} - l_{473})$ and $4(l_{659} - l_{473})$.

By take account these considerations and Eq. 3.2.3 and 3.2.3, we have:

$$ln(\frac{I_j}{I_{0j}}) = -4\Delta l_j \cdot \sum_{i=1}^{n-1} l_j c_i \varepsilon_{i,j} - 4 l_j c_n \varepsilon_{n,j}, \quad j = 1, 2, \ldots s \tag{3.2.5}$$

The relations I_j/I_{0j} are the relative spectral attenuation coefficiens - intensity from the region of skin pathology and surrounding skin (the reference).

If we aim at mapping of skin bilirubin, oxy-hemoglobin, deoxy-hemoglobin and melanin, the following lasers to be suitable: (Table3.2.1). Two illumination wavelengths sets (and two snapshots) could be used in this case, e.g. 415-533-660 nm and 448-533-660 nm laser lines.

This approach can be extended to simultaneous illumination by 5 spectral lines, enabling to map 5 chromophores by a double-snapshot (e.g., additionally beta-carotine). Eventual sets of the illumination laser lines in this case might be 415-532-660 nm and 415-448-590 nm.

Proposal for mapping of more than 3 chromophores by the monochromatic spectral imaging technique was submitted as a patent application.

Table 3.2.1: The parameter values for skin chromophore calculations

j	λ nm	Δl	l cm^{-1}/M	ε_{HbO2} cm^{-1}/M	ε_{HbD} cm^{-1}/M	$\varepsilon_{bilirubin}$ cm^{-1}/M	$\varepsilon_{betacarotine}$ cm^{-1}/M	$\varepsilon_{melanin}$
1.	415	$l_1/2$	104	523080	353222	34903	82223	2359
2.	448	$l_2 - l_1$	139	67044	173320	54336	136270	1935
3.	533	$l_3 - l_1$	348	45400	41336	101	1801	1170
4.	589	$l_4 - l_1$	522	17082	29700	31	1490	805
5.	660	$l_5 - l_1$	678	319.6	3226.56	30	454	541

3.2.4 Results and discussion

Monochromatic spectral images of the colour targets and skin tissue were extracted from the RGB image data cube with respect of the RGB crosstalk correction, as described previously [2], [6]. Measurements of different colour targets at single- and three-wavelength illumination confirmed versatility of this approach.

Equations 3.2.1 and 3.2.2 were used to calculate the values of three chromophore relative concentrations at each image pixel as functions of the measured signals, with subsequent construction of three chromophore distribution maps. As example, Fig.3.2.5 illustrates the obtained results by the first device for two skin malformations – vascular (upper row) and pigmented (lower row). Both distributions qualitatively agree with the expectations from the physiological point of view.

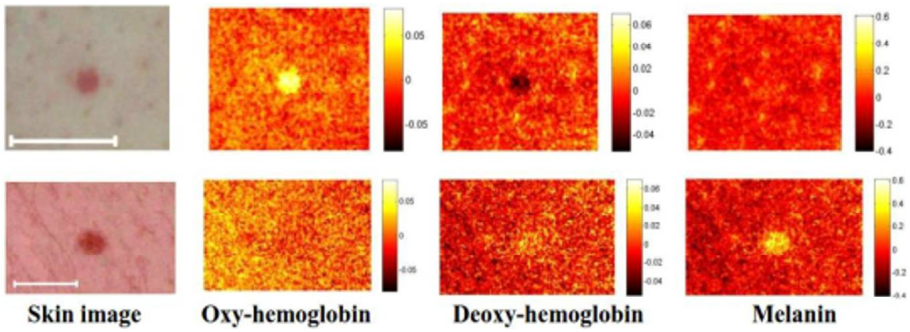

Figure 3.2.5: Maps of skin chromophore distributions for a vascular (upper row) and pigmented (lower row) skin malformations (the scale bar – 1 cm)

Another example where both pigmented and vascular pathologies are on the same image is provided on Fig.3.2.6. One can expect that epidermal melanin concentration in the pigmented lesion would increase if compared with the adjacent skin, without substantial changes in concentration of hemoglobin. As for the vascular pathology, increased oxy-hemoglobin level due to enhanced blood supply is expected with a correspondingly decreased deoxy-hemoglobin level (relatively to the healthy surrounding skin), while the epidermal melanin content does not changes substantially. That was observed clinically as shown in Fig.3.2.6.

One more experimental examination of the developed image processing technique was performed by means of occlusion tests. The middle finger arteries were occluded using a tight resin ring, while the two adjacent fingers were normally supplied with blood; the middle-finger data before occlusion were used as reference. Fig.3.2.7 shows the recorded changes of middle finger chromophore content before, during and after the occlusion. Decreased oxy-hemoglobin content during occlusion was observed, without essential changes in the melanin content, which is physiologically feasible. Immediately after occlusion, a pronounced overshoot of oxy-hemoglobin content in skin was registered (as in similar tests performed by other authors) and a corresponding decrease of deoxy-hemoglobin content with respect to the non-touched skin regions (Fig.3.2.8)

As can be seen, after applying of the cuff there were significantly reduced hemoglobin concentration, due to oxygen deficit the blood. During occlusion the concentration of deoxy-hemoglobin almost remains unchanged. After removing the cuff the the hemoglobin concentration increases rapidly, but concentration of deoxy-hemoglobin quickly falls. Over the time, the concentration of both hemoglobin and deoxy-hemoglobin becomes stable and the same as the beginning of the experiment. Similar results were described in the earlier work developed

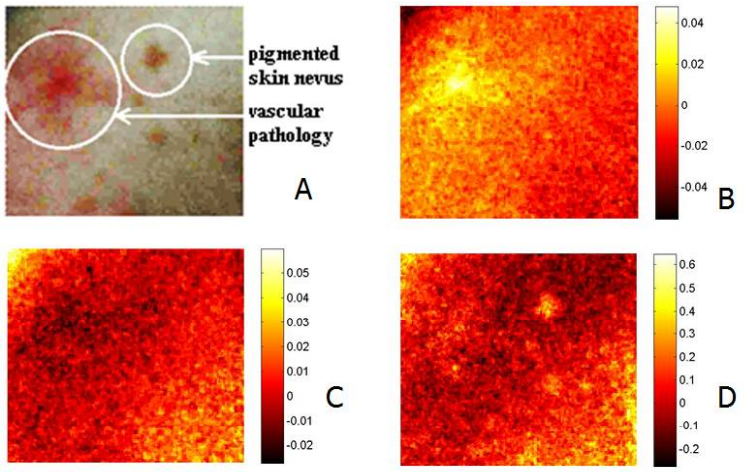

Figure 3.2.6: The maps of skin chromophore distribution in the case when pigmented and vascular pathologies are examined simultaneously: A – RGB image, B – oxy-hemoglobin, C – deoxy-hemoglobin, D – melanin

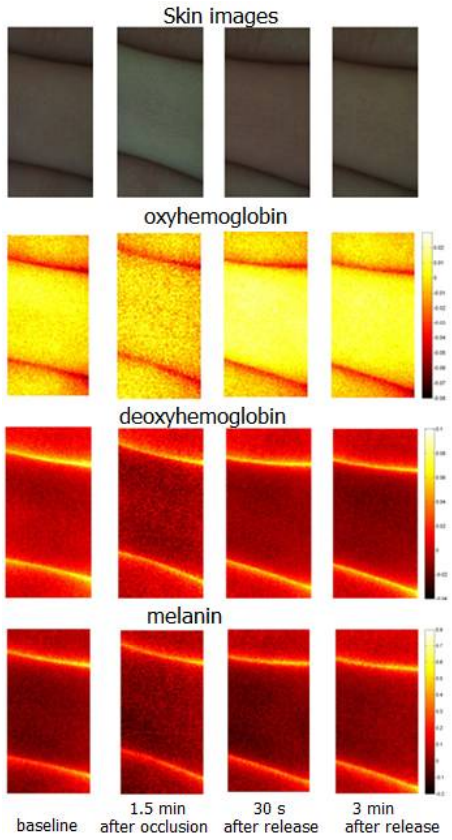

Figure 3.2.7: Changes of middle-finger skin chromophore content in result of occlusion

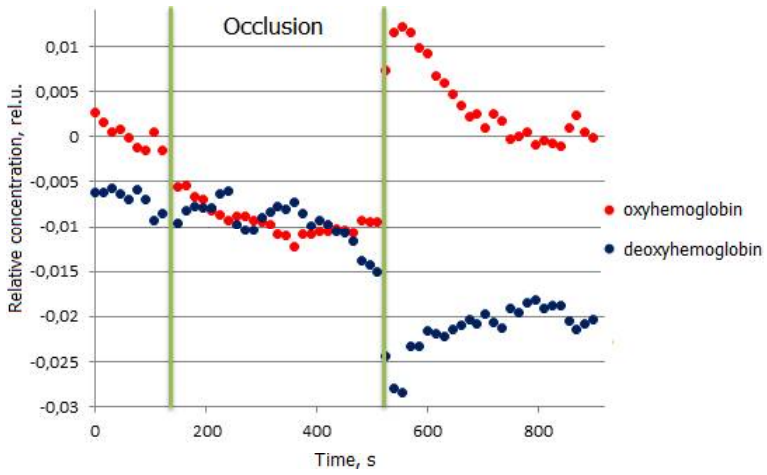

Figure 3.2.8: Relative changes in contents of skin oxy- and deoxy-hemoglobin during the occlusion test

in our laboratory [7].

These scientific results were published in open access article[8], presented in 5 international conferences[9][10][11][12][13], and patented in Latvia[14].

This topic has been defended as Bachelor thesis: Oshina, I. (2015), „Mapping of skin chromophores at tri-chromatic laser illumination", University of Latvia, supervisor Prof. J.Spigulis.

Scientific importance of the results

Possibility to extract three monochromatic spectral images from a single digital RGB image with further conversion into distribution maps of three main skin chromophores was demonstrated for the first time. This technique considerably speeds-up, simplifies and improves accuracy of the procedure of chromophore mapping in dermatology, oncology, microscopy, artwork expertise and other related areas.

Chapter 3.3

Methodology for non-contact monitoring of cardiovascular parameters in the near-infrared spectral range

3.3.1 Introduction

Video imaging technology in the near-infrared (NIR) spectral range for contactless monitoring of cardiac and circulatory parameters was developed as a continuation of proprietary solutions [15], [16] and published works [17], [18] in the field of photoplethysmography imaging (PPGI). The main principle of the method is detection of weak blood flow pulsations from the subcutaneous skin at reflected light with a video camera, using specially developed algorithms and software that amplify and extract the photoplethysmogram signal. This approach opens up many interesting possibilities of potential application, including monitoring of the effect of regional anesthesia (RA) during the surgical operations [19]. Until now, for monitoring of RA the white or green light was used for skin lighting (blood containing hemoglobin has a high absorption in the green part of the spectrum), but the main interest is to perform such monitoring in the infrared part of the spectrum which is invisible - such as security systems, lie detectors or sleep monitoring. The camcoders with RGB image sensors have built-in filters that cuts the radiation in the near-infrared spectral range 0.7-1.1 microns, but it is possible to remove these filters or use monochrome wide-band-visible spectra camera for operating at NIR spectral range.

For implementation of PPGI technology we have developed stabilized narrowband infrared illuminators (GaAs-based LEDs, emission maximum at 760 nm) with the low-noise monochrome video camera equipped with pass-band NIR filter. We developed special video processing software for calculation of photoplethysmogram signal and hemodynamic parameters from the video. Moreover we developed the methodology for real-time visualization of such parameters during the taking of video from skin.

3.3.2 The prototype devices

3.3.2.1 The prototype device for PPG imaging

During of this period the prototype PPGI device was developed (Fig.3.3.1). The device comprises of the body (4x4x4 cm cube, printed by 3-D printer), in which inside there are the following electronic parts: 1) small monochrome video camera (IDS uEye UI-1242LE) for registering video from skin area; 2) NIR ring type illuminator (12 LEDs, 760nm, 20mW each) for uniform illuminating of skin area; 3) LED drivers for supply LEDs with stable current (<300 mA); 4) in the front of LED ring and camera there are placed NIR optical filter and crossed palarizers. LED power control is provided via a USB connection from the computer by means of software. The recording of video frames is performed by the *uEye* software, which captures the video stream in high quality MJPEG format video file.

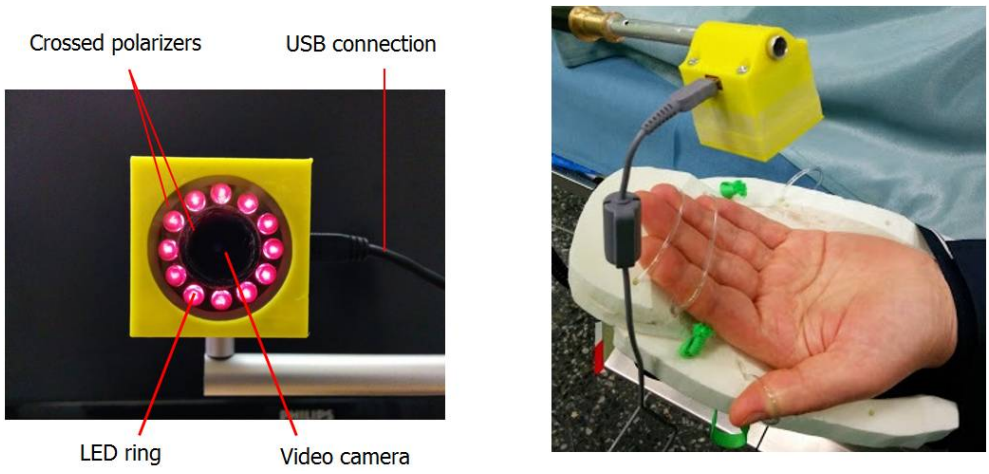

Figure 3.3.1: The PPG imaging device

PPGI device captures the video stream from the skin and transfers it to the computer. For better synchronization of heartbeat detection from the PPGI signal, the contact photoplethysmogram (PPG) was measured simultaneously with the video recording. Contact PPG sensor used in this experiment was custom-made, previously developed and used in IAPS laboratory. The contact PPG signal was transferred to computer via bluetooth and recorded in WAV format by custom-developed computer program.

The experimental setup is shown in Fig.3.3.1. The PPGI video and PPG signal were simultaneously registered by video camera and PPG sensor. The palm was fixed by hand support for minimizing any motion during the experiments. Inside the support the PPGI device was placed with the distance 10 cm from the palm.

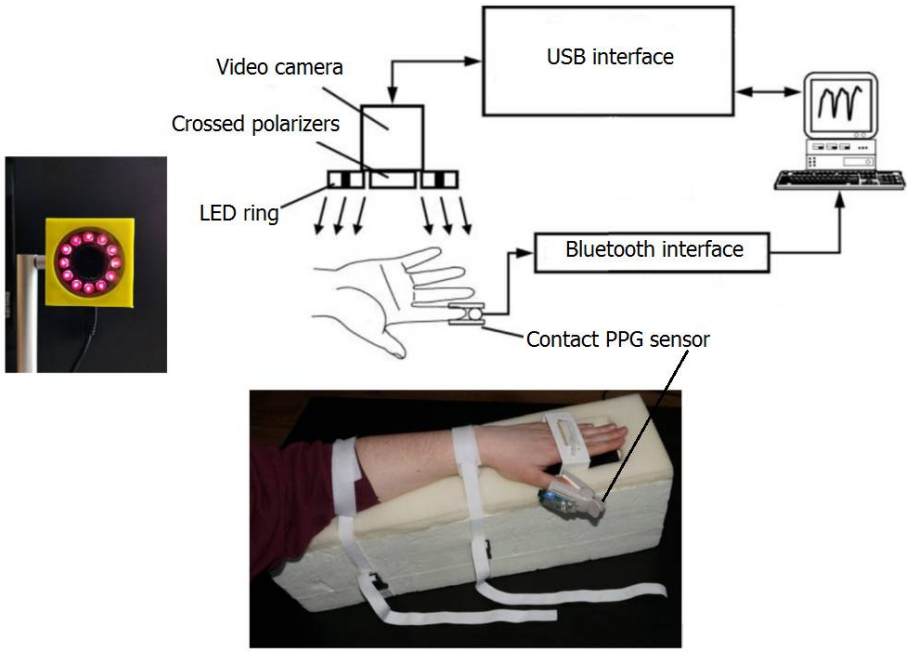

Figure 3.3.2: The experimental setup

3.3.2.2 The prototype device for real-time PPG imaging

During the second period of project we have developed improved version of PPGI prototype device (Fig.3.3.3. During the development of this device, we took into account that the device must meet the following requirements:

- the video should be with high frame rate for getting quality PPG signal;
- the video should be with high dynamic range and low noise level to get quality PPG signal;
- the field of view should be large enough and the image should not be distorted by geometric abberations of lense;
- the intensity of LEDs should be high enough to provide sufficient lighting at high frame rate of video;
- the light source should provide uniform illumination of palm skin during the measurements;
- the prototype device should be portable and convenient for using in clinical environment.

During the second period of project, we worked on a development of improved prototype device, which includes the technical concept, the choosing of precise design elements, the design of an electronic circuit and electronic circuit boards. During this work, first the electronic circuit board, which fulfills all needs of this device, was developed. Then the electronic circuit board was designed and

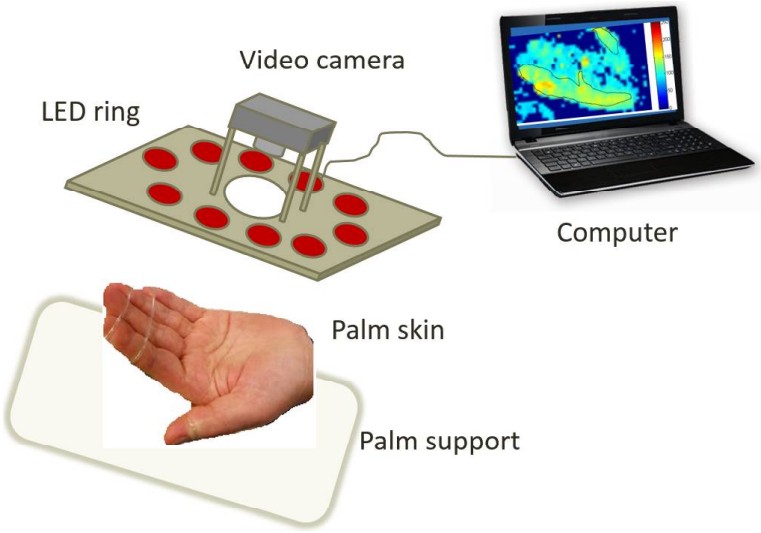

Figure 3.3.3: The concept of prototype PPGI device

all electronic components were placed virtually. The circuit board also provides the heat transmission from the high power LEDs. The block-diagram of PPGI device is shown in Fig.3.3.4.

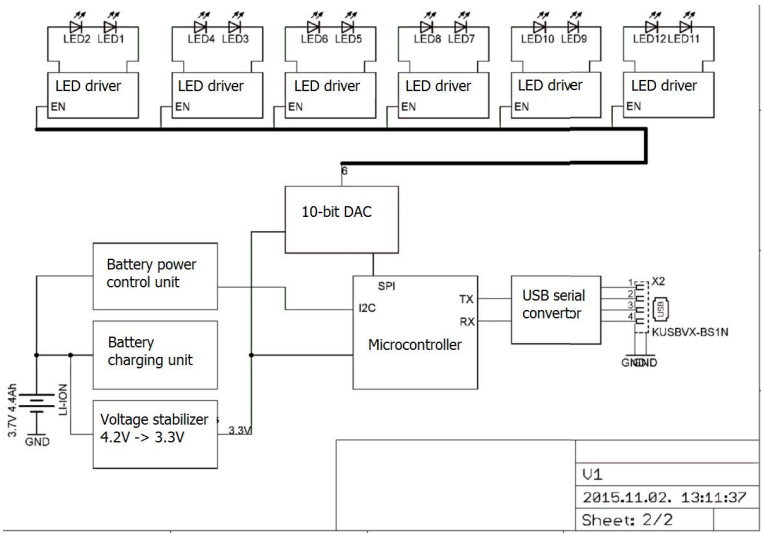

Figure 3.3.4: The block-diagram of PPGI device

The size of board is 100mm x 150mm (Fig.3.3.5), the shapes of board are rounded. There are 12 NIR LEDs placed around the video camera which is in the centre of board. The LEDs (SMB1N-760D no www.roithner-laser.com) are high-power high efficiency light sources (400mW optical power each, 760nm, wide angle light). On the opposite side of board there are placed cooling radiators for cooling of LEDs. The precise intensity control is performed by high quality 12-bit DAC (TLV5632IPW - Texas Instruments).

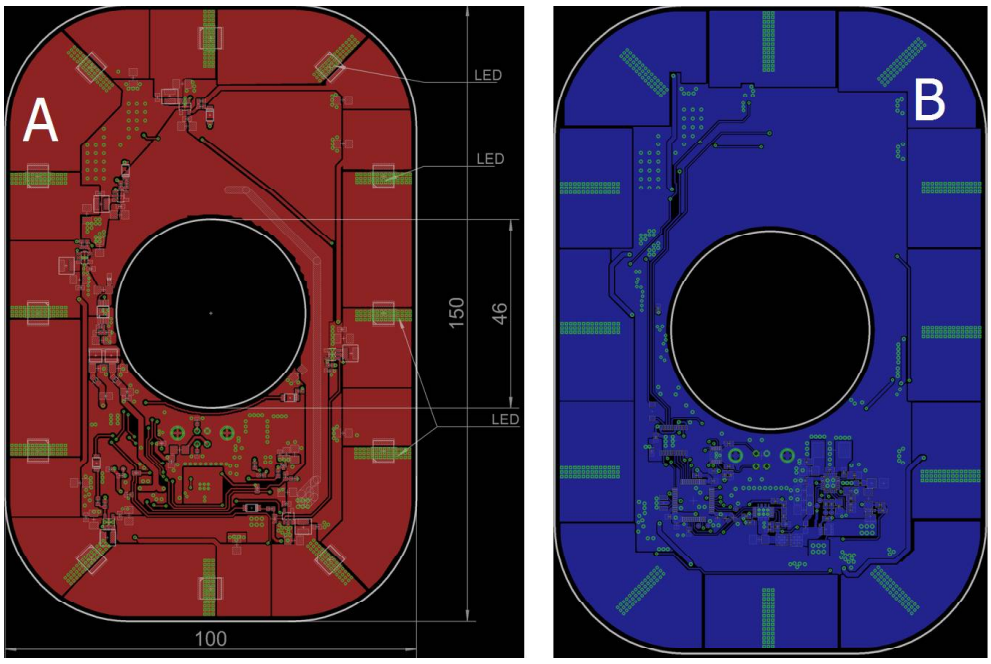

Figure 3.3.5: Drawing of the PPGI device: component side (left) and the other side (right)

The embedded the lithium-ion battery charging circuit (BQ24278 - Texas Instruments), which operates in impulse mode, provides fast battery charging (less than 2 hours). The built-in battery pack (4.4 Ah) provides continuous measurement at least at one hour.

Device control is provided via the USB port, which also provides battery charging when the device is not working. The battery capacity monitoring circuit calculates battery life in real-time. Thus, the user will be informed about the maximum measurement time when the battery charge is enough. Microcontroller provides communication among all electronic blocks, processing and transferring of data. In the center of board there is a hole for video camera with C-mount lens, which is mounted on the board.

3.3.3 Algorithms and software for PPGI processing

3.3.3.1 The calculation of hemodynamic parameters from PPGI

During the first period of project the PPG analysis algorithm and computer program was developed. The algorithm (Fig.3.3.6) allows to perform fast offline analysis of large video data and perform analysis of PPG signals and several hemodynamic parameters (pulse rate, pulse amplitude and phase). The software allows to choose two regions of interest (RoI) from the skin video and the time interval within the PPG signal.

Skin blood microcirculation analysis software is based on the following algorithm (Fig.3.3.6):

1. Video frames are loaded and stored as 3-D matrix data (WxHxframes);

2. Two PPG signals are calculated from the chosen RoIs;

3. The PPG signals are filtered, so the pulsatile (AC) component is obtained (heart activity, 0.7-2 Hz) and slow varying component (DC) is obtained (0.01-0.1 Hz);

4. The hemodynamic parameters are calculated in every heart beat (pulse rate, pulse amplitude, DC value and pulse transit time (PTT) between two RoIs).

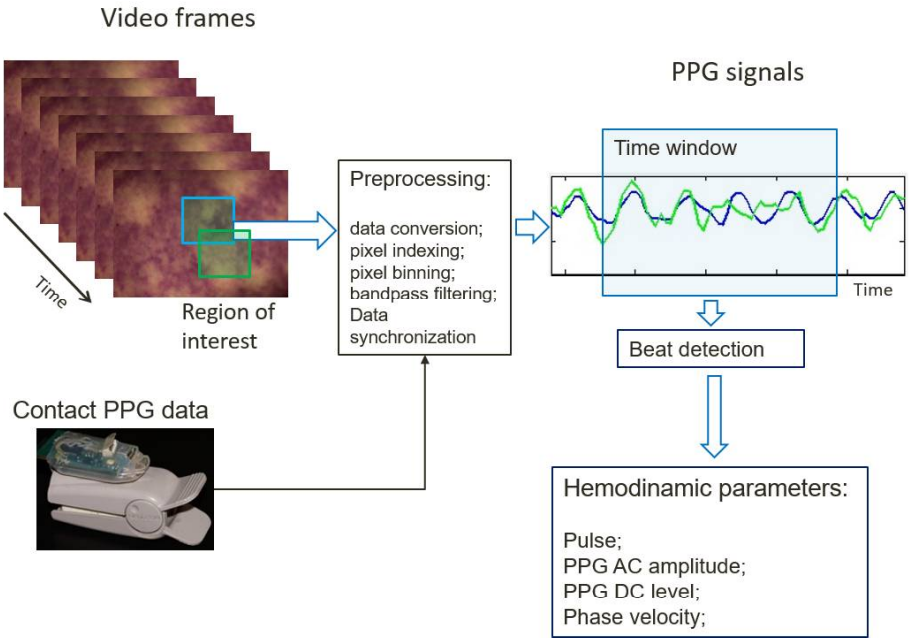

Figure 3.3.6: The block-scheme of PPGI analysis algorithm

The software is developed in Matlab environment, the Graphic User Interface (GUI) is shown in 3.3.7. The software allows to load skin video and data from PPG contact-sensor. The software allows interactively choose two RoIs by mouse click, from which the PPG signals are calculated and displayed. This signal can be filtered by adjustable band-pass and low-pass filters. The Fourier spectra of PPG signals is calculated and displayed. The user can interactively choose the time interval within the PPG data from which the hemodynamic parameters are calculated. These data can be exportet to Mat format for later analysis.

For the more detailed analysis of hemodynamic data the analysis software module was developed 3.3.8. The software calculates and displays statistical data: correlations among PPGs and among several hemodynamic parameters (pulse rate, AC amplitude, DC amplitude, phase shift and PWTT between the two RoI of skin). This module was used for analysis of hemodynamic parameters of palm micro-circulation during the warming experiments.

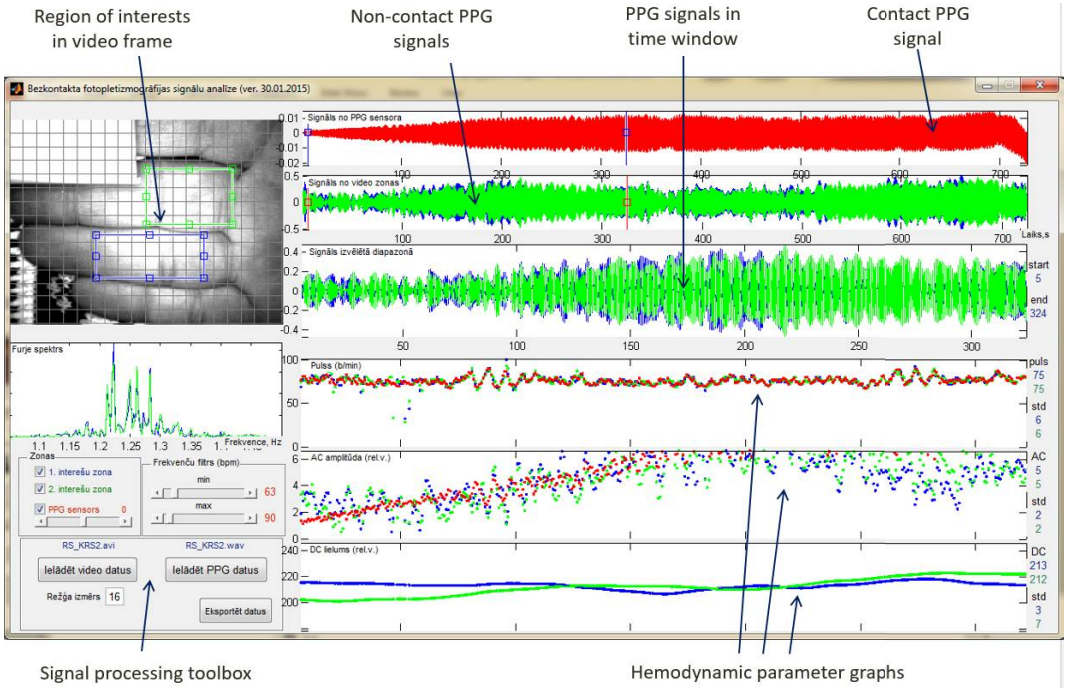

Figure 3.3.7: The graphic user interface of PPGI analysis software

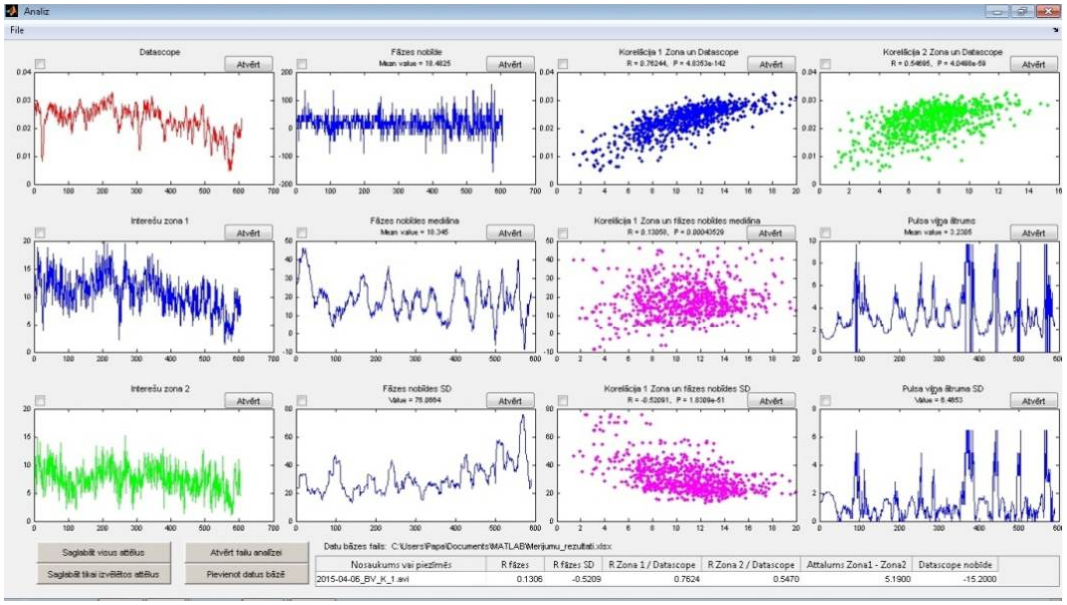

Figure 3.3.8: The graphic user interface of analysis of hemodynamic parameters

3.3.3.2 The software for real-time photoplethysmography imaging for the monitoring of effect of regional anesthesia

The algorithm

During the second period of the project, the real-time PPGI monitoring algorithm and software was developed. The previously developed algorithm was improved and realized in MATLAB GUI. The hemodynamic parameters (AC amplitude) can be calculated in every pixel of video image and can be visualized as parametric 2-D map. Moreover, the software is able to calculate the parametric map in real-time. This approach allows to monitor the spatial distribution of blood flow during the measurements.

The PPGI algorithm is based on a spatio-temporal video analysis and analysis of blood volume pulsations in skin. The algorithm is based on the following steps:

1. Video frames are obtained from video camera or from previously recorded video file. Each video frame is converted from *uint*8 to *double* format data and stored to the data array.

2. In order to improve the quality of PPG signal first the decomposition of each video frame is performed. The set of images are calculated from the original frame: images with 1/2, 1/4, 1/8 ... of its original size. When the image resolution decreases, it contains a progressively lower frequency components. Image decomposition is used by Gaussian pyramid recursively formula:

$$\begin{aligned} &G_0(x,y) = I(x,y), \text{for initial frame,} \\ &G_k(x,y) = \sum_{m=-2}^{2}\sum_{n=-2}^{2} w(m,n)\cdot G_{k-1}(2x+m, 2y+n), \text{for downsampled images,} \\ &k = 0, 1, \ldots N \end{aligned} \tag{3.3.1}$$

where $I(x,y)$ is initial frame, $G_k(x,y)$ - decomposed k-level image, x,y – spatial coordinates; N - decomposition level; $w(m,n)$ kernel function, which is defined by following way:

$$w(m,n) = \frac{1}{16}[1,4,6,4,1] \tag{3.3.2}$$

3. In the next step the image restoration is performed by superposition of image sets by using different weight coefficients c_k for images with different spatial frequencies. The resulted image contains amplified low-frequency components, which overall improve PPGI signal quality:

$$X(x,y) = \sum_{k=0}^{n} c_k \cdot G_k(x,y), \tag{3.3.3}$$

4. For the extracting of pulsatile AC component of PPG signal the pass-band frequency filter is used, which is tuned to the cardiac frequency range of 0.7-2 Hz. Filtering is performed in the each pixel of image, resulting image is obtained from the previous 5 frames:

$$\begin{aligned} Y_n(x,y) = 0.006 \cdot X_n(x,y) - 0.012 \cdot X_{n-2}(x,y) + 0.006 \cdot X_{n-4}(x,y) \\ +3.7278 \cdot Y_{n-1}(x,y) - 5.2542 \cdot Y_{n-2}(x,y) + 3.3194 \cdot Y_{n-3}(x,y) \\ -0.7935 \cdot Y_{n-4}(x,y) \end{aligned} \tag{3.3.4}$$

where $Y(x,y)$ is current image at n-th video frame. Filtering Band-pass filtering is performed by 2nd degree IIR Butterworth filter. The main advantage of IIR filter is similarity and computing inexpensiveness which allows a real-time calculations.

5. The AC amplitude map is calculated in every pixel of image. The AC amplitude is calculated as root mean square (RMS) amplitude of PPG signal. We are using recursively formula to obtain the SUM matrix from previous frames:

$$\begin{aligned} &S_0(x,y) = 0, \text{ if } n \leq B \\ &S_n(x,y) = S_{n-1}(x,y) + Y_n(x,y)/B - Y_{n-B}(x,y)/B, \text{ if } n > B \end{aligned} \tag{3.3.5}$$

where S is RMS amplitude in the buffer, B is buffer length.

Resulting amplitude is obtained by subtracting the current signal from *zero* level:

$$A_n(x,y) = S_n(x,y) - Z \tag{3.3.6}$$

where Z is *zero* level of PPG amplitude, which can be calculated as: $Z = min[A]$

The software

During the second period of project we have developed a computer program for real-time PPGI mapping. A computer program was developed in Matlab environment, and is intended for operating the PPGI prototype device and real-time skin perfusion monitoring and analysis. The software GUI has been adapted to work with the tablet PC, it was approved at the IAPS lab and Traumatology and Orthopedics Hospital patients for monitoring of regional anesthesia effect before the surgical manipulation. Computer software user interface consists of the following main components:

1. Control panel of PPGI device, LEDs and video camera, which include LED intensity adjustment and exposure control of camera;

2. The measurement mode buttons, for setting the time moments when the doctor perform some kind of manipulations;

3. Info panel with current process indication (current time, timer, temperature of video sensor, CPU memory level, etc.);

4. Left window shows the current frame of video with two RoIs polygons; right window shows PPGI amplitude map in indexed colors;

5. Middle window displays the RoI-averaged PPG amplitude signals with the time mark positions (doctor's manipulations).

6. Current frame/time positioning slider, which allows "move in time" when the off-line PPGI analysis is performed (after the ending of current measurement).

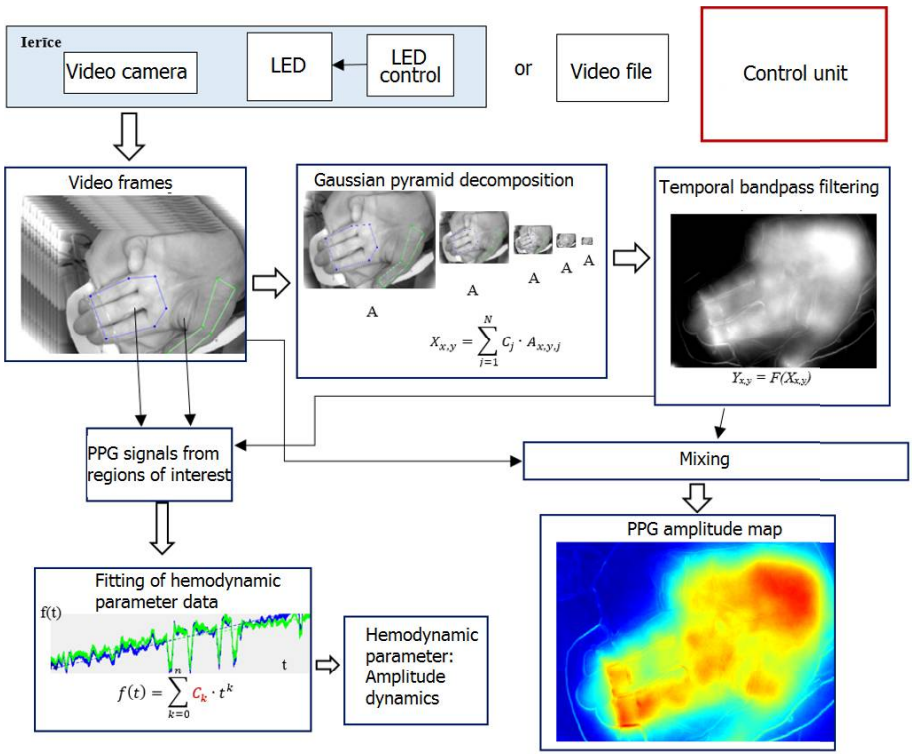

Figure 3.3.9: The block-scheme of real-time PPGI algorithm

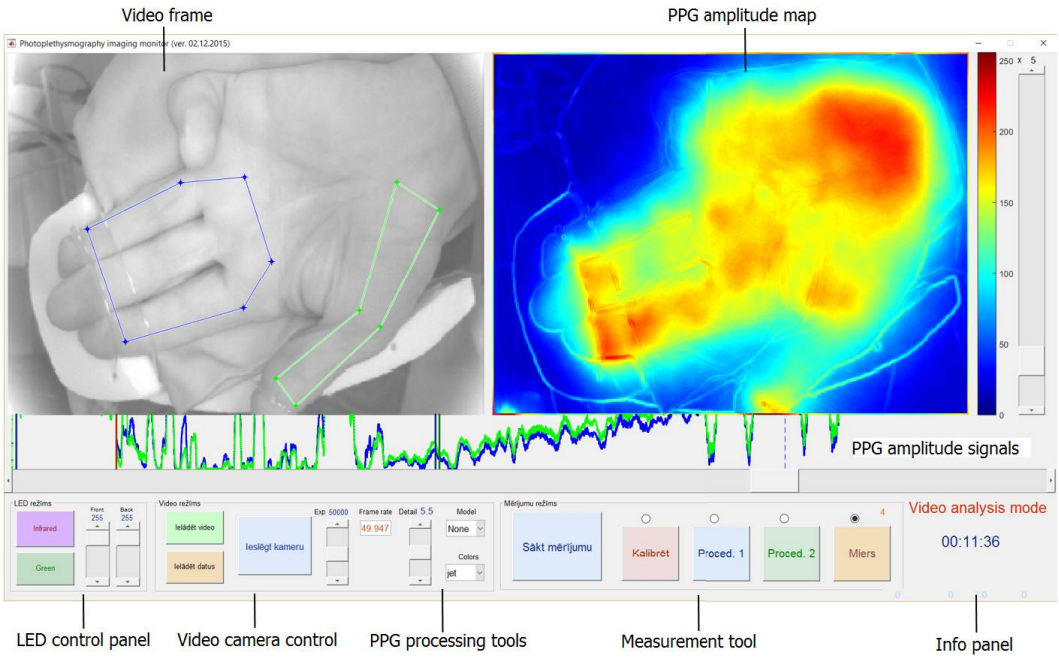

Figure 3.3.10: The graphic user interface of real-time PPGI

3.3.4 Results and discussion

3.3.4.1 The analysis of hemodynamic parametrs

The PPGI technology at the NIR wavelength band around 760nm was developed and tested in laboratory and clinic. 24 volunteers (12 women and 12 men, 20-35 years old) were involved in the measurement series with permission of the local ethics committee. Wrist was selected as the most suitable body location for such measurements (Fig.3.3.2). The contact PPG signal at the NIR spectral band was used for reference.

3 measurements every 10 minutes were taken from both wrists – one was fan-heated, the other at room temperature. All data were collected at a database for further analysis. The schematic of experimental setup is given on (Fig.3.3.2). Our previously designed wireless PPG finger clip was used for parallel contact measurements.

During the analysis the dynamics of following hemodynamic parameters were analyzed: 1) contact PPG AC amplitude, 2) PPGI AC amplitude un 3) pulse wave transit time (PWTT) calculated from two RoI of palm skin. The measurement results were presented in 12 different groups:

1. female group, heating with termophore, PWTT;
2. female group, heating with termophore, PPGI AC amplitude;
3. female group, heating with termophore, contact PPG AC amplitude;
4. female group, heating with hairdryer, PWTT;
5. female group, heating with hairdryer, PPGI AC amplitude;
6. female group, heating with hairdryer, contact PPG AC amplitude;
7. male group, heating with termophore, PWTT;
8. male group, heating with termophore, PPGI AC amplitude;
9. male group, heating with termophore, contact PPG AC amplitude;
10. male group, heating with hairdryer, PWTT;
11. male group, heating with hairdryer, PPGI AC amplitude;
12. male group, heating with hairdryer, contact PPG AC amplitude;

The PPG AC amplitude and PPGI AC amplitude from both RoIs were synchronized in every heartbeat cycle. The PWTT were calculated from these parameters from 5 heartbeat cycles as the average value.

The results show that the PWTT depends on temperature effects (Fig.3.3.11. In first minutes of experiment, the hairdryer provides faster warming of the palm than the thermophore. The results showed that experiments with hairdryer leads to faster increasing of PWTT than in experiments with thermophore. Similarly, PPG AC signal amplitude increased faster when a hairdryer was used. Both contact and contactless PPG measurements showed similar results (Fig.3.3.12, $R > 0.7$).

Scientific importance of the results

The PPGI technology currently uses mainly visible (e.g. white, green) illumination of the subject; this causes some essential problems (e.g. influence of changes

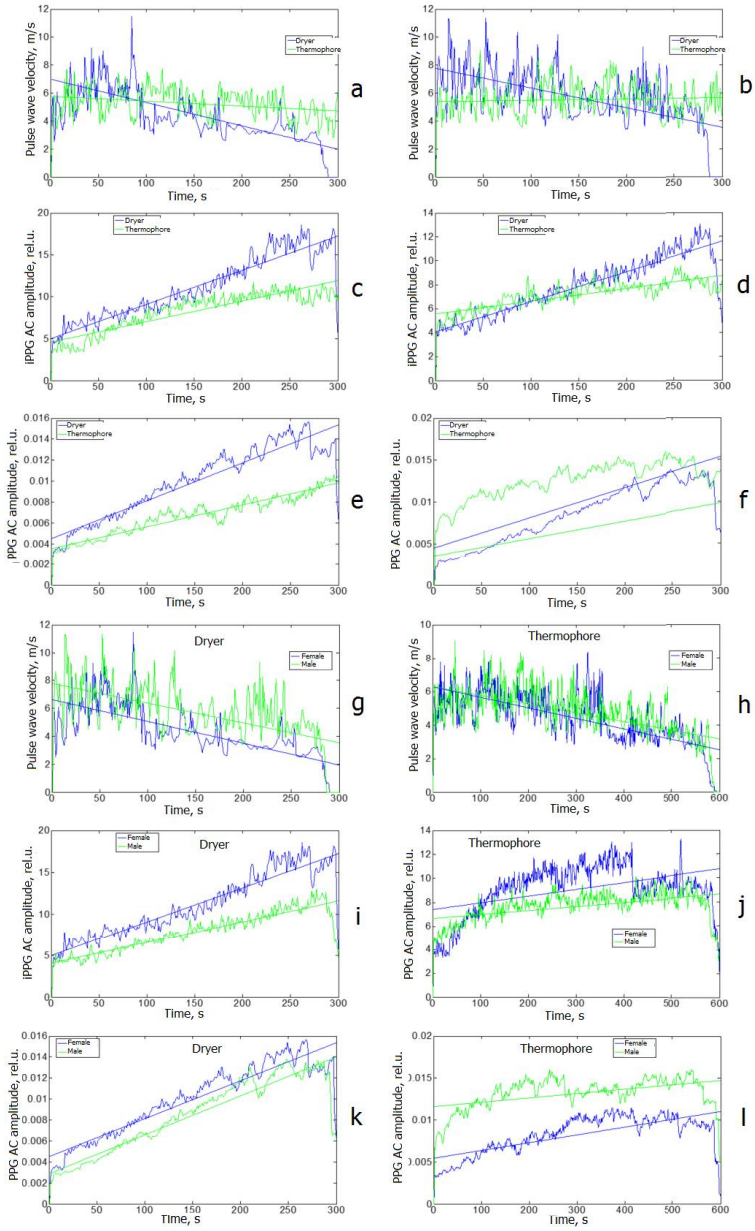

Figure 3.3.11: The correlation among the hemodinamic parameters during heating tests: (a,c,e) female group, (b,d,f) male group, (g-l) comparison between female and male group

in ambient light, sensitivity dependence on skin colour, useless for secure monitoring of cardiovascular parameters). Extending this technology to NIR spectral range considerably diminishes or even avoids these issues so opening new application areas in clinical medicine, physiology and security sensing.

This topic has been defended as Master thesis of Physics at the University of Latvia: Olga Ļashuka. „Determination of pulse wave velocity by the non-contact photoplethysmography method", (Supervisor Dr. Uldis Rubīns.).

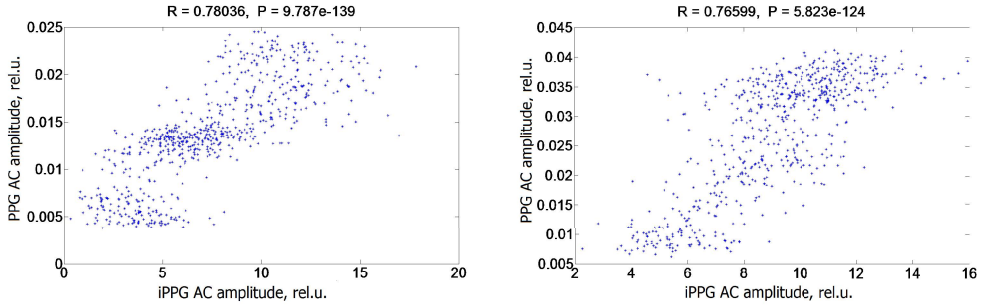

Figure 3.3.12: The correlation between the contact-PPG and PPGI amplitudes. Data points were calculated from single heartbeats

3.3.4.2 The analysis of PPGI and thermal images for monitoring the effect of regional aneshesia

For the first time the thermal imaging (FLIR C2) was tested in a clinical environment of Traumatology and Orthopedics Hospital and clinic OrtoMed in Latvia. The PPGI technique was tested in these clinics previously. We validated these both techniques together for better monitoring of RA effect during local anesthetic procedure.

The FLIR measurements were performed on the different skin areas to obtain skin temperature distributions during 1) regional anesthesia of hands and palm areas; 2) spinal anesthesia - the feet; 3) as well as verification of the spinal neural pain blockades - on the feet areas.

The PPGI measurements simultaneously with FLIR measurements were performed during the hand palm (*plexus brachialis*) RA procedure. One measurement was performed when the anesthetic was administered near the *ulnaris* nerve (one of the four nerves) in the underarm area. The innervation of *ulnaris* nerve causes the dilation of vascular bed and temperature increasing of some areas of palm. Both FLIR Thermography and PPGI mapping technology showed a similar increasing of blood flow in the palm area immediately after input of local anesthetic (Fig.3.3.14).

The thermography system shows high sensitivity and specificity of unilateral bed temperature control of the anesthetic effect. Results showed high sensitivity of detecting blood circulatory changes during the RA which obtained by temperature distribution measurements by FLIR thermo camera. Thermal data were compared with PPGI data, and there was confirmed good agreement between the two methods for monitoring of palm anesthesia effectiveness.

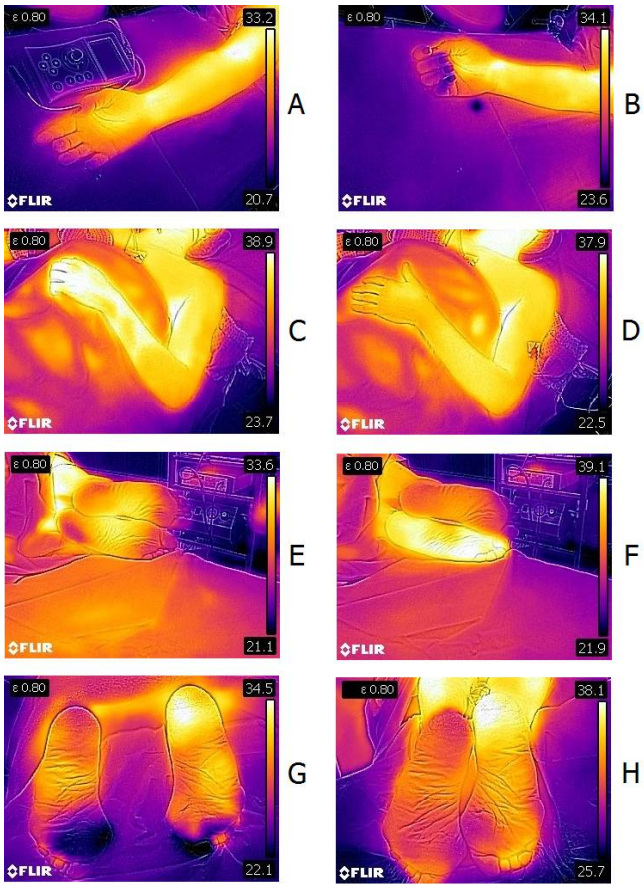

Figure 3.3.13: The comparison of FLIR thermal images before (left) and after the RA procedure (right). (A-B) lower hand - RA effect almost is not visible; (C-D) upper side of palm - successful RA effect; (E-F) feet during spinal anesthesia - successful effect of RA; (G-H) feet during spinal blockade - successful effect

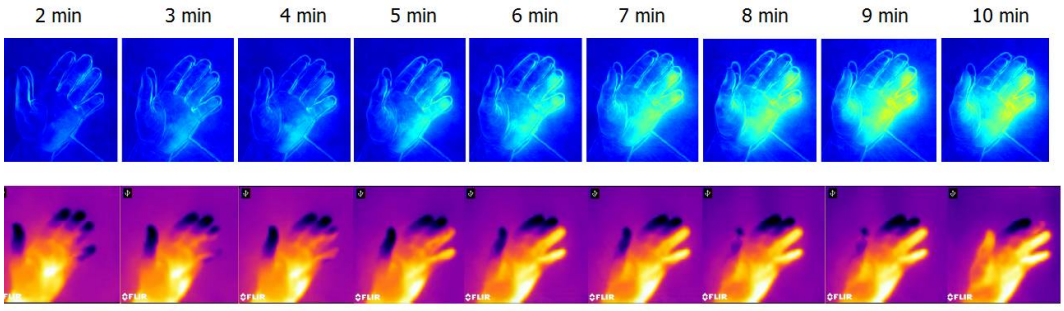

Figure 3.3.14: The comparison of PPGI amplitude maps (above) and thermal images of palm (images below) after the *plexus brachialis* RA procedure (time moments 2-10 min after local anesthetic input)

Chapter 3.4

Methodology for assessment of skin moisture and its distribution in the infrared spectral range

3.4.1 Introduction

Near-infrared reflectance spectroscopy has a potential for noninvasive estimation of skin moisture (volume fraction of water in skin) as there is a high water absorption in this spectral range of 900-1700 nm. This is very important for cosmetic industry, for example, for measuring the effect of different moisturizing creams on skin, as well as for medical purposes. Although previous studies by other groups show that with a near-infrared detector with sensitivity up to 2.5 μm it is possible to distinguish even small changes in skin hydration, these types of InGaAs detectors are much more expensive and inaccessible than detectors up to 1.7 μm sensitivity. In the spectral range up to 1.7 μm there are also water absorption maxima that could possibly be used for determination of skin hydration, thus this spectral range should be explored further, which is what we have been studying in our group.

During this period, we have developed methods and laboratory devices for estimation of skin moisture by near-infrared reflectance spectroscopy, as well as near-infrared imaging. We have tested both devices in laboratory, and we have tested the reflectance spectroscopy device in clinics. During the clinical measurements, we also compared our developed device with a commercially available device for estimation of skin moisture. During this period, we also did Monte Carlo simulations to better understand how different optical properties of skin affect the diffuse reflectance spectrum of skin in this spectral range.

3.4.2 Background

There are three distinct water absorption peaks in the near-infrared spectral range of 900-1700 nm: 980 nm, 1200 nm, and 1450 nm. In addition, also lipids and collagen absorb electromagnetic radiation in this spectral range[20]; however, their absorption can be considered much weaker than that of water. In this spectral range, both Mie and Rayleigh scattering takes place, so the total scattering can be considered as a sum of both scattering regimes. It is known that scattering decreases by a power law with increasing wavelengths[21].

There are currently commercially available devices for estimation of skin moisture based on electrical properties of skin (conductance, resistance) - with increased water volume in skin (increased skin moisture) there is increased skin conductance. The development of optical methods for estimation of skin moisture has been quite slow, mostly, because the detectors in the near-infrared spectral range are quite expensive. However, there is a reason to believe that in the nearest future the price for those detectors will decrease, thus advancing research in this field[22].

3.4.3 Related work

There is a huge variety of different moisturizers, lotions and other products that supposedly reduce skin dryness. However, it is not clear how much effect these products actually give in short and long term. Currently, commercially available devices (e.g. Corneometer, Skicon, Nova, etc.) for determination of skin moisture level are based on electrical properties of skin (conductance, capacitance). Studies show good correlation between results acquired by different commercially available devices[23]. However, these techniques are indirect as the given result is related not only to the level of skin moisture but also the surface state (contact impedance between the skin and the electrode can vary depending on skin roughness) and the thickness of stratum corneum (SC) that varies between different body parts[24].

There are studies on the near-infrared reflectance spectroscopy as a technology for determination of in vivo skin moisture level from the 1990s. In 1993, Martin suggested a method to quantitate water on a relative basis to distinguish free, bulk and bound water, as well as additionally using scattering off the skin surface as a measure of skin smoothness[25]. In 2005, Suh et al presented work of doing in vitro skin moisture measurements on hairless mouse, as well as in vivo skin moisture measurements on human inner arm by FT NIR spectrometer. They used partial least squares regression to develop a calibration model by comparing near-infrared reflectance spectroscopy results to the conventional capacitance method[26]. In 2006, Iwasaki et al introduced a NIR spectral imaging system consisting of an indium gallium arsenide (InGaAs) NIR camera, halogen bulb light source and optical filters (1060 nm and 1450 nm) to differentiate skin where a moisturizer has been applied[27]. In 2011, Egawa et al suggested an imaging system for analysis of both water and oil content in facial skin by using a sensitive InGaAs NIR camera in the spectral range 1100-2200 nm which was

also able to acquire images of skin at 1920 nm which is the strongest water band in this spectral range. They suggest that at 1920 nm it is possible to detect even small changes in water volume fraction in skin[28].

3.4.4 Our approach

3.4.4.1 Device for estimation of skin moisture by near-infrared reflectance spectroscopy

The experimental setup comprised a near-infrared spectrometer (Ocean Optics, NirQuest 512) in the spectral range of 900-1700 nm, Y-type water free (WF) optical fiber probe, tungsten-halogen light source (Thorlabs SLS201/M), and a 3D printed nozzle as a spacer to separate skin from the detection and illumination fibers (Fig.3.4.1). Optical fiber probe consisted of 6 illumination fibers in a circle around 1 detection fiber in the middle without any space between fiber ends. The distance between optical fiber ends to the skin surface of interest was kept constant of 5 mm by the nozzle (outer diameter 25 mm, inner diameter 4 mm). During measurements, the room temperature was kept at 23°C. The room was dark to avoid any disturbances; however, a dark spectrum was always subtracted from all measurements. The reflectance spectrum was converted to absorption spectrum by using the light source irradiation spectrum $I_0(\lambda)$ which was acquired as the reflectance spectrum of an almost ideal white reference tile (Avantes WS-2) in the spectral range 350-1800 nm.

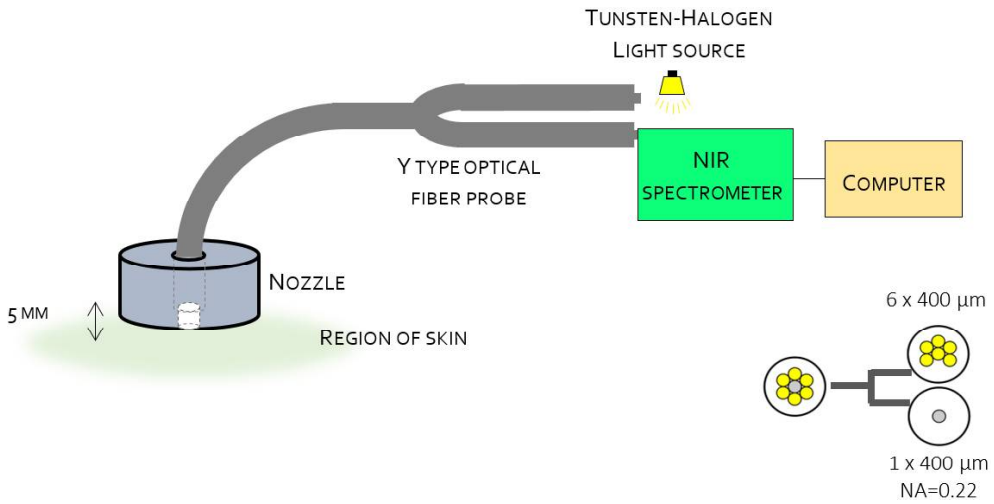

Figure 3.4.1: Device for estimation of skin moisture by near-infrared reflectance spectroscopy

Experimental validation and data analysis

Experimental validation of the device was done by acquiring reflectance spectra of human skin in vivo. Typical skin absorption spectrum in the near-infrared spectral range in comparison with water absorption spectrum is shown

in Fig.3.4.2. For a better comparison, water absorption is shown in normalized values, and skin absorption is represented by optical density (OD) values, normalized in such a way that OD value at 900 nm is 0. OD values that represent absorption are calculated as:

$$OD(\lambda) = log\frac{I_0(\lambda)}{I(\lambda)} \tag{3.4.1}$$

where I_0 is the light source irradiation spectrum taken as the reflectance spectrum of an almost ideal white reference tile, and I is the reflected intensity by skin.

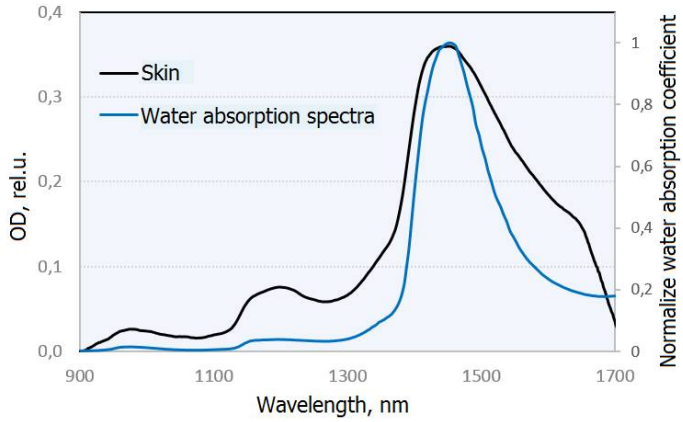

Figure 3.4.2: Comparison of measured skin absorption (OD) spectrum and water absorption spectrum

Experimental validation was done by acquiring absorption spectra over time after application of a moisturizing cream on their forearms. This was done to estimate the ability of the developed device to obtain changes in skin moisture over time assuming that the application of a moisturizing cream increases skin moisture. Fig.3.4.3 shows results of one example - a moisturizing cream (Neutrogena fast absorbing hand cream, light texture) was applied on the forearm of a female (26 years old, skin type II), and OD spectra were acquired each 10 seconds just after the application of the cream. For easier data presentation and interpretation, 3 wavelengths which correspond to the water absorption maxima were chosen: 980 nm, 1200 nm, and 1420 nm. Change of OD value at all three wavelengths over time is shown in 3.4.3.

As we can observe in 3.4.3, OD value at 1420 shows the most visible change over time, which was expected as it corresponds to the spectral range that water absorbs the most in this range. We can also observe that there is a rapid increase in OD value during the first minute after application of the cream. During the next 4 minutes OD value decreases quite rapidly until it reaches a value that stays constant for the last 5 minutes of this experiment. However, this is only one example for one volunteer, and in other cases OD value change over time showed different patterns. There are different factors which can affect

the results: what the moisturizing cream consists of, each volunteer's skin can absorb the moisturizing cream in a different manner, and the layer of the cream that is applied on skin surface could have differed a bit for each volunteer. Up until now, we have not come up with a method for applying the same amount and thickness of the cream layer for each measurement so that we could have comparable measurements.

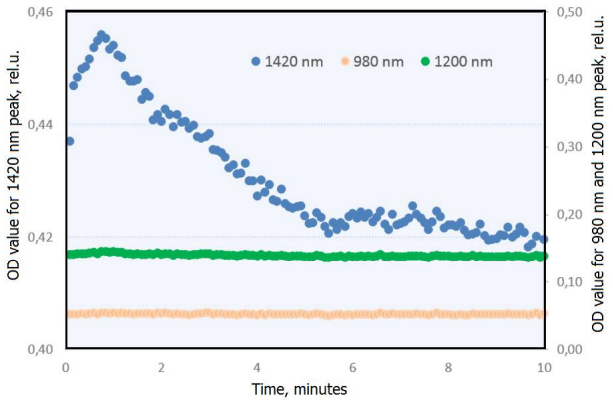

Figure 3.4.3: Example of OD value changes over time after application of a moisturizing cream for 3 wavelengths that correspond to water absorption maxima: 980 nm, 1200 nm, and 1420 nm.

3.4.4.2 Device for estimation of skin moisture by near-infrared imaging

Another device was developed for mapping of skin to distinguish between regions with increased water volume fraction and normal skin. It consisted of an 8-bit 320x256 pixel 8-bit near-infrared camera (Xenics, XS-1.7-320) sensitive in the spectral range of 900-1700 nm, near-infrared bandpass filters of central wavelengths 980±2 nm, 1100±2 nm, 1200±2 nm, 1300±2 nm, 1450±2 nm and 1600±2 nm (Thorlabs), and a halogen lamp light source, directed at a 45° angle in order to eliminate the specular reflection off the skin surface coming directly into the camera (Fig.3.4.4). Transmission spectra of the optical filters are shown in 3.4.5.

Experimental validation and data analysis

Monochromatic 8-bit reflectance $R(x, y)$ images were acquired by the camera, and a simple calculation was used to express absorption at each image pixel:

$$A(x, y) = \frac{1}{R(x, y)} \tag{3.4.2}$$

The developed device was experimentally tested in laboratory measurements. At first, possibilities to distinguish between skin region with applied moisturizing cream on its surface and normal skin were studied. However, results showed no

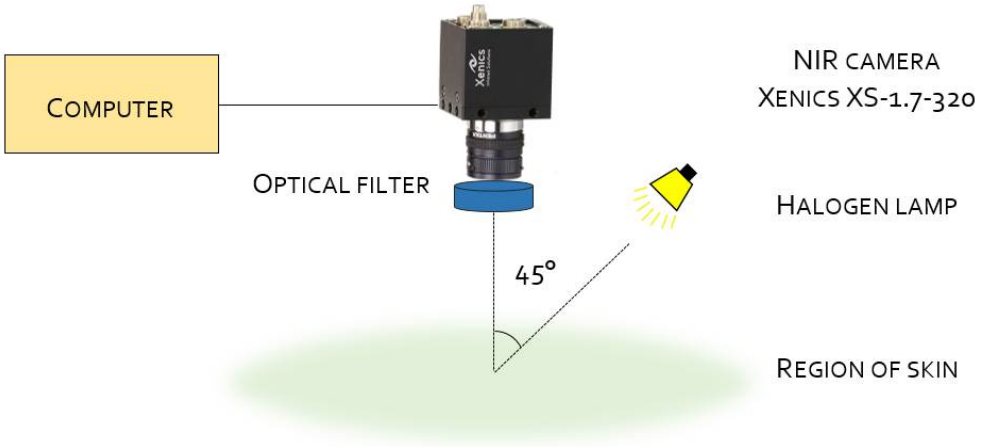

Figure 3.4.4: Device for estimation of skin moisture by near-infrared imaging

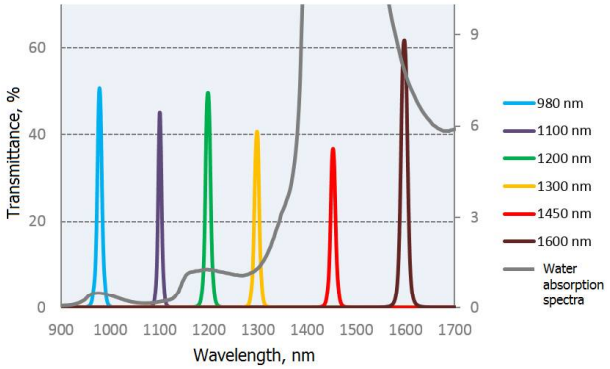

Figure 3.4.5: Transmission spectra of optical filters (Thorlabs), compared to water absorption spectrum

statistical difference between absorption parameter A when comparing moisturized and normal skin regions, thus a conclusion was made that it is not possible to detect small changes in skin moisture (for example, by applying a very small layer of moisturizing cream on skin surface), as it was expected. In the future, we are planning to improve the developed device by using a better illumination from different sides at the same time, by filtering out visible light illumination so that only near-infrared illumination is used, as well as by advancing the dynamic range of the images.

Even though we concluded that with the developed device it was not possible to distinguish skin regions with increased moisture due to applied moisturizing cream on skin surface, we saw that it was possible to distinguish skin regions with noticeably more water content in them. More specifically, we did notice considerable change in absorption parameter A between a blister and surrounding normal skin. The blister was around 1 mm in both thickness and diameter, and blisters normally consist of mostly water. 3.4.6 shows the 6 spectral ab-

sorbance images (taken using 6 different filters) of a hand with blister in almost the middle of it. The images were analyzed in the following way: in each spectral absorbance image, a region of the blister was selected, and a region of the surrounding normal skin was selected. Then, the average absorbance A value was calculated out of all selected pixels of each selected region of skin. 3.4.7 shows a closer look of 2 spectral absorbance images (980 nm and 1450 nm), and red line represents the border of the blister. Fig.3.4.8 shows the calculated average absorption parameter A for each of the 6 spectral ranges of blister and normal skin. As we can observe from Fig.3.4.8, absorption parameter values depending on wavelength look similar to the water absorption spectrum, as expected. In addition, absorption parameter A has higher values for blister than normal skin, especially, at wavelength 1450 nm. These results show that the developed near-infrared imaging device can be used for distinguishing between regions with increased water volume fraction; however, at this moment it is only possible to detect regions with considerably higher water volume fraction than the surrounding normal skin.

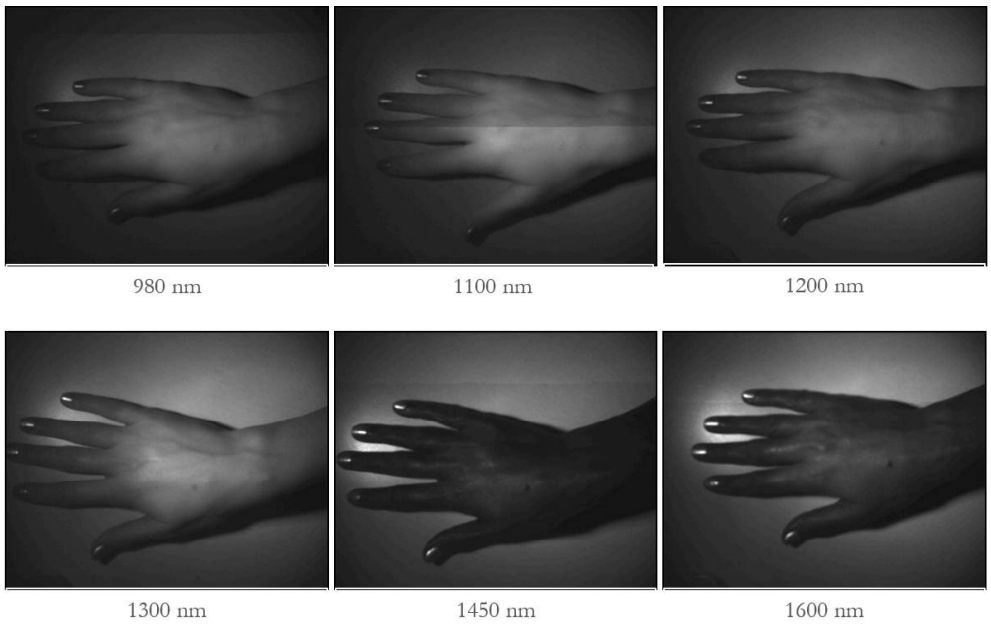

Figure 3.4.6: Six spectral absorbance images of a hand with a blister almost in the middle of it, acquired by the developed near-infrared imaging device

Figure 3.4.7: Close-up images at 980 nm and 1450 nm, the red line shows the border of the blister

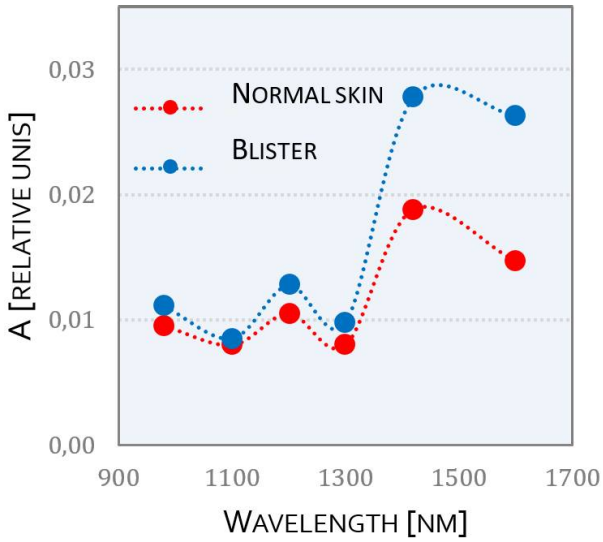

Figure 3.4.8: Average absorption parameter A dependence on wavelength of normal skin and blister

3.4.5 Clinical validation of the developed device for skin moisture estimation by near-infrared reflectance spectroscopy

3.4.5.1 The measurements

The developed device for estimation of skin moisture by near-infrared reflectance spectroscopy was validated in clinical measurements. During January and February, 2016, clinical measurements of 39 volunteers were performed in collaboration with dermatologists at the professor J. Kisis' clinic in F. Sadovnikovs Str. 20, Riga, Latvia. All volunteers gave a written consent before participating in this

study.

The goal of this study was to test long-term effect of a moisturizing cream X and serum Y on skin moisture level. Participants of this study were using the moisturizing cream X on the proximal part of volar aspect of the left arm (closer to the elbow), and the moisturizing serum Y on the dorsal part of volar aspect of the left arm (closer to the palm) every day for one month. On the contrary, they were asked not to use any cream or serum on the volar aspect of the right arm for the whole month .

At each of the three regions of interest (dorsal part of left arm, proximal part of left arm, and right arm) 3 separate measurements were performed to calculate the average value at each of the three regions of interest. Measurements were performed in the beginning of January and in the beginning of February – one month later, to compare the effect of the cream X and serum Y on skin moisture level. Average moisture level values in the beginning and one month later of each of the three regions of interest were compared.

Measurements were performed by two different devices – the developed device for estimation of skin moisture level by near-infrared spectroscopy, and a commercial device DermaLab (by Cortex Technology) which estimates skin moisture level based on changes in skin conductance (with increased water volume fraction in skin, there is an increase in electrical conductance of skin). Measurements were performed at similar conditions for all 39 volunteers.

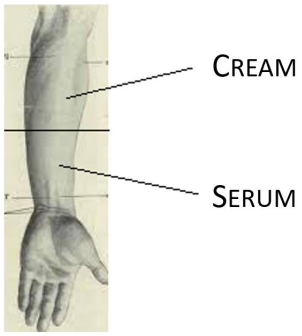

Figure 3.4.9: The volar aspect of an arm: moisturizing cream was applied on the proximal part (closer to the elbow) and moisturizing serum was applied on the dorsal part (closer to the palm)

3.4.5.2 Data analysis

Absorption spectra (OD values) in the spectral range of 900-1700 nm were acquired at each measurement, and for further analysis only OD value at 1450 nm was used as during the experimental validation it proved to be the most sensitive to changes in moisture level. OD values at 1450 nm were in the range of 1.5 to 1.8 [relative units] for all 39 volunteers. For easier data analysis and comparison, an empirical method was used for calculation of a parameter representing skin moisture: 10^{OD}. Thus, relative skin moisture level values for all 39 volunteers were in the range 30 - 70. In comparison, skin moisture values acquired by Der-

maLab were in the range 30 - 300 (micro Siemens, μS), which shows us that for little increase in skin moisture, DermaLab skin moisture values increase more rapidly than in case of the developed near-infrared spectroscopy device.

At first, an analysis was performed to test if relative skin moisture values of one region of interest of all 39 volunteers at one temporal measurement are normally distributed. It was done by performing a Lillifors statistics test in Matlab. If two datasets are normally distributed, a Two sample T Test can be performed on both datasets to test whether there is a statistically significant difference between them. For example, whether there is a statistically significant difference between the dataset of relative skin moisture values of dorsal part of the left arm in January and in February for the whole group of 39 volunteers. It was expected that there should be no significant difference between both temporal measurements for the control group (the right hand), and there should be significant difference between both left hand groups: the proximal part where the moisturizing cream X was being applied, and the dorsal part where the moisturizing serum Y was being applied for one month.

3.4.5.3 Results

In total, results were divided in 5 groups for each device (10 groups in total), where each group consisted of skin moisture values for all 39 volunteers:

- Right arm (control) group in the beginning;
- Right arm (control) group 1 month later;
- Left arm group in the beginning;
- Left arm cream group 1 month later;
- Left arm serum group 1 month later.

To perform the Two sample T Test, at first an analysis was performed to test whether all group datasets are normally distributed by Lilliefors statistics test. Results showed that 8 out of 10 groups were normally distributed; however, 2 were not: DermaLab results of the left arm cream group 1 month later, and DermaLab results of the right arm (control) group 1 month later. As an example, Fig.3.4.10 shows histograms of results acquired by the developed near-infrared spectroscopy device (on the left) and by DermaLab (on the right); results of the right arm (control) group 1 month later are presented in this figure. However, Two sample T Test was still performed also by using these 2 of 10 groups that did not show normal distribution; it only means that the test results can be less reliable than in the case were data in a group are normally distributed.

The following values were also obtained for analysis of the results:

- Average value of skin moisture level for all volunteers 1 month after minus average value of skin moisture level for all volunteers in the beginning: V;
- Standard deviation (the distribution of all results in one group): STD_V;

- Standard error: $SE_V = STD_V/\sqrt{N}$, where N is the amount of volunteers (39) in one group.

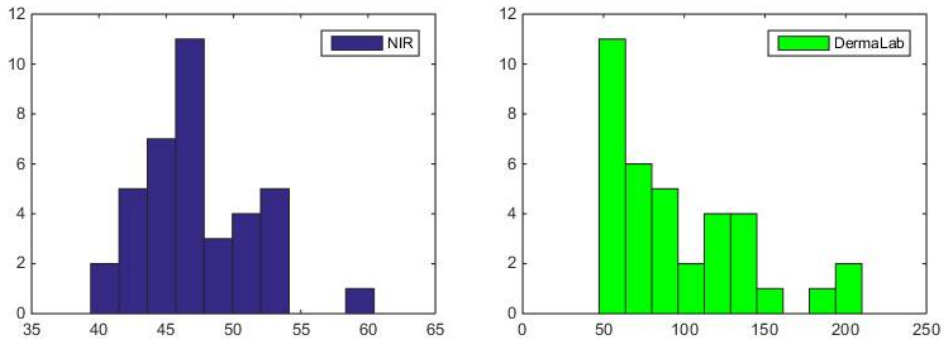

Figure 3.4.10: Histograms of skin moisture parameter values for right arm (control) group 1 month later by the developed near-infrared spectroscopy device and by DermaLab

Two sample T Test gave the following results:
1. By the developed near-infrared spectroscopy device:

- Comparison of right arm (control) group data in the beginning and 1 month later gave the conclusion that there is no statistically significant difference ($p = 0,80$) between both groups; $V = 0$; $STD = 4$; $SE = 0,6$; $N = 38$.

- Comparison of left arm cream group data in the beginning and 1 month later gave the conclusion that there is no statistically significant difference ($p = 0,18$) between both groups; $V = -1$; $STD = 6$; $SE = 0,9$; $N = 38$.

- Comparison of left arm serum group data in the beginning and 1 month later gave the conclusion that there is statistically significant difference ($p = 0,03$) between both groups; $V = 2$; $STD = 5$; $SE = 1$; $N = 38$.

2. By the commercial DermaLab device:

- Comparison of right arm (control) group data in the beginning and 1 month later gave the conclusion that there is statistically significant difference ($p = 0,04$) between both groups; $V = 18$; $STD = 43$; $SE = 7$; $N = 36$.

- Comparison of left arm cream group data in the beginning and 1 month later gave the conclusion that there is statistically significant difference ($p < 0,05$) between both groups; $V = 61$; $STD = 49$; $SE = 8$; $N = 36$.

- Comparison of left arm serum group data in the beginning and 1 month later gave the conclusion that there is statistically significant difference ($p < 0,05$) between both groups; $V = 35$; $STD = 47$; $SE = 8$; $N = 36$.

3.4.5.4 Conclusions

It was expected that there should be no statistically significant difference between right arm (control) groups in the beginning and 1 month later, and such a result was obtained by the developed near-infrared spectroscopy device. By subtracting the average relative skin moisture value of all volunteers (38) 1 month later from the average value in the beginning, the result was $V = 0$. However, the standard deviation of V was relatively high: $STD_V = 4$. On the other hand, by using DermaLab results, we concluded that there is no statistically significant difference between both groups, which is not what we expected.

When comparing cream and serum groups, results by the developed near-infrared spectroscopy device showed that there is no statistically significant difference between cream group in the beginning (before starting to use the cream) and 1 month later. However, results showed statistically significant difference between serum group in the beginning (before starting to use the serum) and 1 month later, even though the improvement $V = 2$ is not very high. When comparing cream and serum groups with the commercial device DermaLab, we concluded that for both, cream and serum, there is statistically significant difference between data in the beginning and 1 month later. In addition, in case of the cream, the improvement is around two times higher ($V = 61$) than in case of the serum ($V = 35$).

In conclusion, we can observe that DermaLab is more sensitive to small changes in skin moisture than the developed near-infrared spectroscopy device, and it is possible to evaluate the effect of cream and serum on skin moisture level 1 month after using them. However, by using DermaLab we also got results that we did not really expect – there was a statistically significant improvement also for the control (right arm) group. Maybe it is due to the fact that some volunteers actually used moisturizing creams or lotions on the right arm even though they were asked not to, or maybe there were other factors affecting those results, for example, the outside temperature, physiological aspects etc.

3.4.6 Monte Carlo simulations for analyzing the effect of different optical parameters on reflectance spectrum in the near-infrared spectral range

A graphic user interface was developed in Matlab programming tool for easier use of Monte Carlo simulations (Fig.3.4.11). Description of the developed program:

- The user can choose the wavelength range of interest in the total spectral range from 250-1700 nm; spectral resolution can be chosen as well;
- The user can choose the amount of photons to be used in simulations which affects the precision of the simulation;
- The user can choose the amount of skin layers to analyze, as well as optical parameters of each of the layer: refraction index, scattering coefficient,

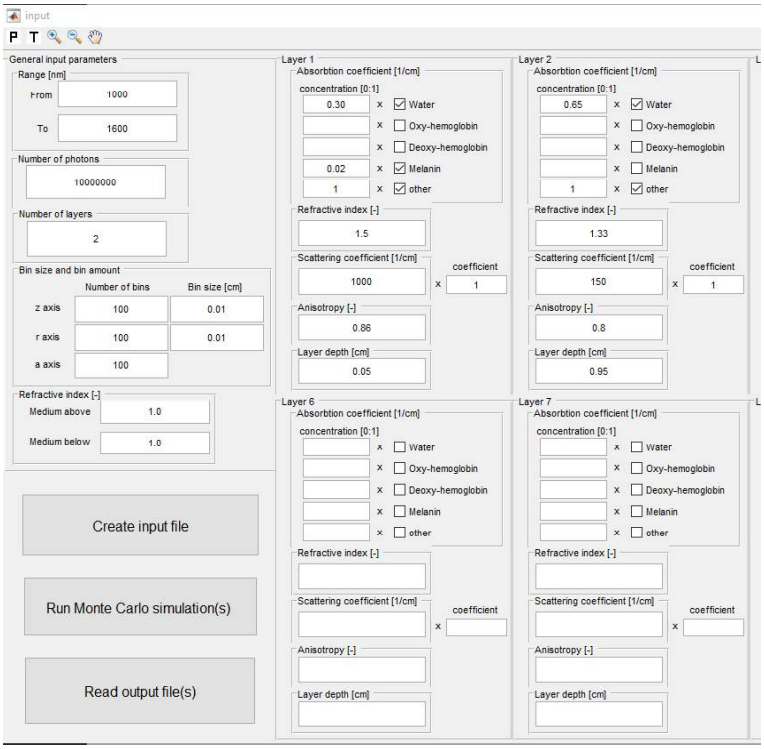

Figure 3.4.11: Screen shot of a part of the user interface of Monte Carlo simulations program

anisotropy factor and layer thickness. The user can choose which chromophores are located in each of the layers and how much volume fraction each of the chromophores occupy. If needed, the user can also modify the absorption coefficient values for respective chromophores and also the equation of how scattering coefficient is being calculated;

- The user can choose the size of the local data grid. In z axis, the grid size should be the same as the total thickness of the skin model;
- The user can set the refraction index of the material (above and below skin);
- The user can choose between two options: use mcml or GPUmcml to do the calculations with; the second one can only be chosen if the user has a suitable graphic card and *CUDA* software;
- When all parameters are set, the program outputs a file that is afterwards used to run the Monte Carlo simulations. Then, the simulation results are given as a table: absorption, specular reflectance, diffuse reflectance and transmittance values depending on the wavelength.

During this project, we also did some other improvements for the developed Monte Carlo simulations program un the graphic user interface:

- Other chromophore absorption coefficient values have been added that absorb in the visible spectral range of 250-1000 nm: melanin, oxyhemoglobin, and deoxyhemoglobin (absorption coefficient values acquired from http://omlc.org/spectra/[29]);
- Two other ways how to calculate scattering coefficient were added[30]:

$$\mu_s = \frac{2 \cdot 10^{12} \cdot \lambda(nm)^{-4}}{1-g}[cm^{-1}] \tag{3.4.3}$$

where μ_s is scattering coefficient, λ is wavelength, g is anisotropy factor[31]:

$$\mu_s(\lambda) = \frac{1.1 - 5.1 \cdot 10^{-4} \cdot \lambda(nm)}{1-g}[cm^{-1}] \tag{3.4.4}$$

- Chromophore absorption coefficient values were approximated with binomial Gaussian distribution functions in Origin software, so that the user can specify the spectral range of interest with a desirable spectral resolution:

$$y_1 = y_0 + He^{-0.5(\frac{x-x_c}{w_1})^2}, y_2 = y_0 + He^{-0.5(\frac{x-x_c}{w_1})^2} \tag{3.4.5}$$

where x - wavelength, H – spectral intensity, x_c - central wavelength of the distribution

w_1 if $x_c < \lambda$, w_2 if $x_c > \lambda$ - function y_1 used for wavelengths shorter than the local maximum at x_C, and function y_2 used for wavelengths longer than the local maximum at x_c. An example of approximation of oxyhemoglobin absorption spectrum by 9 Gaussian functions (red line is the superposition of 9 Gaussian functions, green lines are all the separate Gaussian functions, black line, barely seen as it is just under the red line, shows the absorption spectrum of oxyhemoglobin):

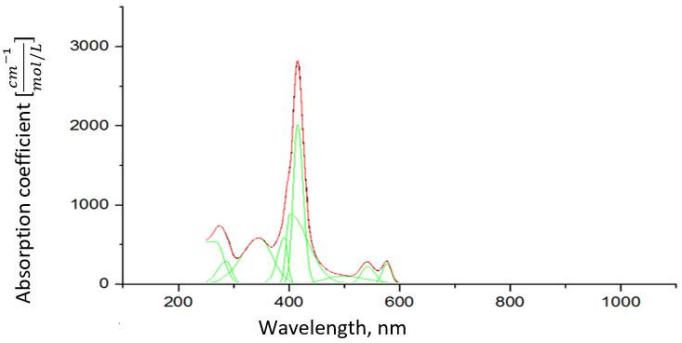

- Another option has been added in the Monte Carlo simulation program: if the user inputs experimental diffuse reflectance spectrum, the program can automatically calculate chromophore volume fraction values within desirable error values. However, graphic user interface has not been developed for this option yet.

Chapter 3.5

Improvements of the multimodal imaging prototype device „SkImager”

3.5.1 Introduction

In the ERDF project 2010/0271/2DP/2.1.1.1.0/10/APIA/VIAA/030 we developed a prototype device for skin multimodal imaging - “SkImager” [32][33] (Fig.3.5.1). Device is intended for optical diagnosis of the skin lesions (melanoma, vascular formations, etc.) and it was designed as simple portable device for doctors-dermatologists. Prototype device was approbated in the IAPS laboratory and in the two dermatology clinics. After consulting with doctors, we found that the device contain some technical failures. This project was intended to Skimager improvement and applies it to clinical requirements.

The device is controlled by the touch screen with built-in mini-computer, which processes CMOS camera captured images and outputs to the display 6 different skin parametric maps. Spectral, fluorescent and microcirculatory imaging using 24 LED ring light, alternately turning on and off 6 different spectral bands of light sources: white light and different radiation spectrum with peaks at 405 nm, 450 nm, 540 nm, 660 nm and 940 nm. Multimodal imaging device control and data processing software is functioning, but it is need of further improvements to make it more clinically informative - for example, it is desirable color calibration of skin chromophore concentrations, contrast improvement in melanoma-nevuses separation image, erythema index calibrated color images, etc. It is important that doctors be able to efficiently take diagnostic conclusions, especially without going into the technical nuances of the device.

In this project we made improvement in the prototype design, optimized electronic and improved firmware.

Figure 3.5.1: Prototype device for skin contact-less diagnostics "Skimager": a) the device in holder, which at the same time charges the battery; b) the device in action

3.5.2 Improvement of mechanical and electronic components

The improvement of the Skimager is defined in the following tasks:

- Optimize electronics circuit;
- To optimize the LED light source wiring diagram;
- Move and improve the power and reset buttons;
- Set the control button on the device grip, for easy control of the device;
- Replace resistive to capacitive touch screen;
- Develop LED ring axial rotation lock;
- Develop a polarizer mount and axial rotation lock;
- Replace the polarizer filters with broadband polarizer;
- Izveidot USB, SD kartes ligzdu un ieslēgšanas pogas padziļinājumus;
- Attach the buzzer;
- Create a passive air cooling within the housing.

Figure 3.5.2: Prototype device "Skimager" and the internal structure of assemblies[33]

In the project we investigated about 10 different possible LED power circuits. The most appropriate solution where found - where each spectrum LED diodes connected in series and the power supply electronics located on the main board. LED voltage increase and current stabilization provides chip MAX1698. It can be set stabilized current level, feeding the control input voltage level. The voltage can be set with the DAC (digital-to-analog converter) LTC2631 chip, which in turn is controlled by a I2C control line from the SkImager CPU.

Improvement of the LED ring electronics includes replacement of LED power supply circuit to DC-DC supply. Previously, the linear regulator large portion of the battery power converted into heat, thus inefficiently using electricity. Replacement of the impulse power supply is technically more correct, and takes full advantage of battery power. After many studies we chose MAX1698 LED driver from the company Maxim. This meets all the required technical parameters. In order to perform the measurements were made the test board (for example, operating modes and power consumption). LED ring will be easily detachable - no connecting wires in case the device will need to be repaired. This solution is simpler and technically more correct.

Also were made other significant improvements, such as device power supply circuit research, which may result in the replacement of the module - schematically simpler, cheaper and more energy efficient. This ensures SkImager devices a longer operating time on one battery charge.

3.5.2.1 LED ring

Schematic diagram of LED ring was completely remade. LED groups are connected in series and created Plug-type connection to the main board. Connecting tracks is maximally wide and occupies the largest possible area, thus providing LED heat transfer. PCB drawing added with three needle-shaped plug-ins that provide UV filter and the polarizer fixation, as well as an easy loading and unloading.

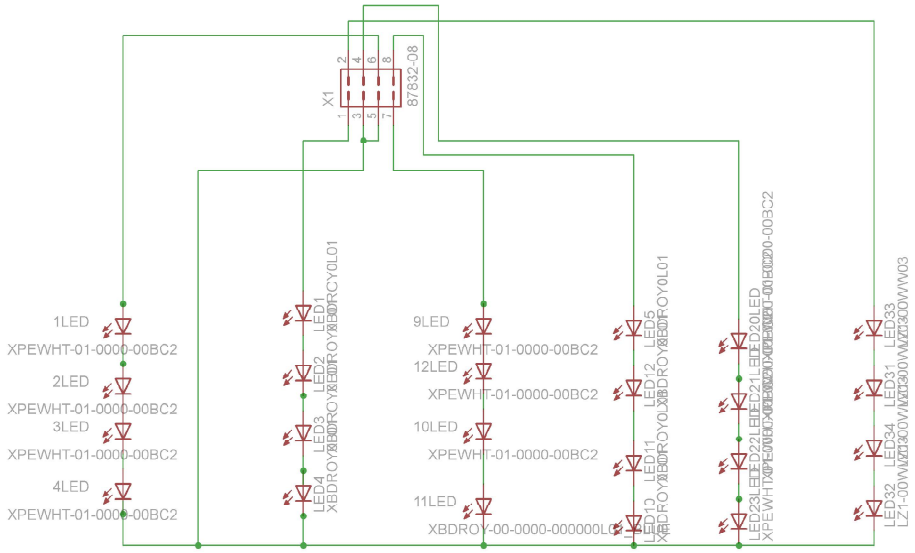

Figure 3.5.3: Schematic diagram of LED ring

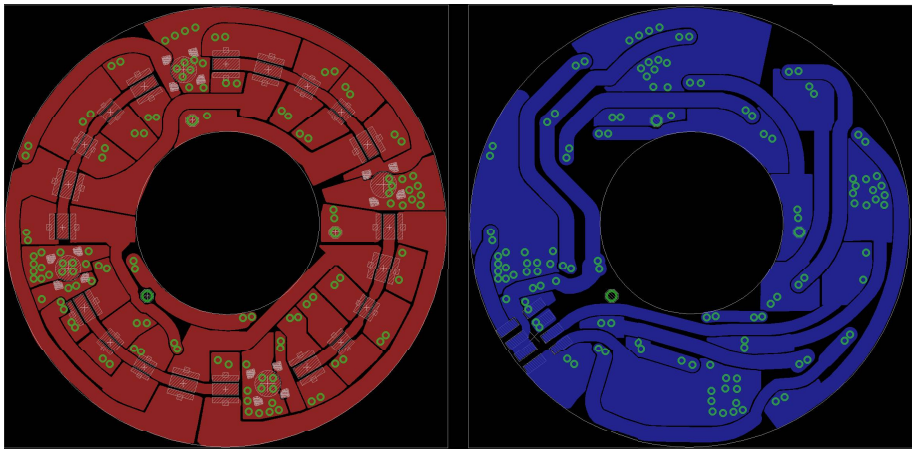

Figure 3.5.4: LED ring drawing: component side (left) and drawing the other side (right)

3.5.2.2 CMOS image sensor

Within the project one of the tasks was to optimize Skimager principal scheme, which also includes a CMOS image sensor. MT9T031 is mounted on a separate double-layer circuit board having a size of 32 x 30 mm. Board was optimized - reduced data line track width and improved by shielding the data lines (places where it is physically possible). Skimager devices CMOS image sensor was chosen MT9T031 from APTINA Imaging. This is 1/2" 3-megapixel sensor with 10-bit parallel interface. More information about the sensor can be found on the manufacturer's specification. Figure shows principal circuit diagram that match the manufacturer's recommendations.

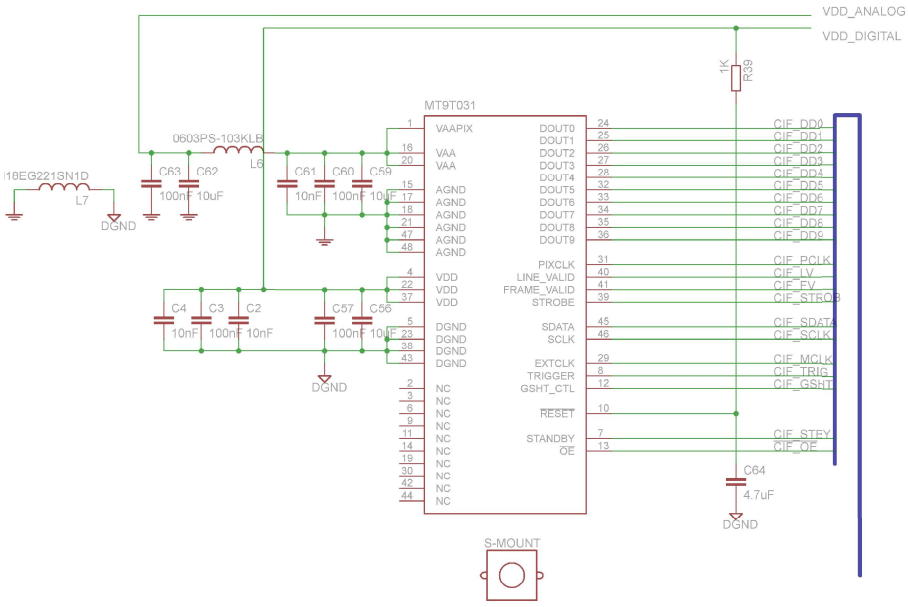

Figure 3.5.5: CMOS attēla sensora principālā shēma

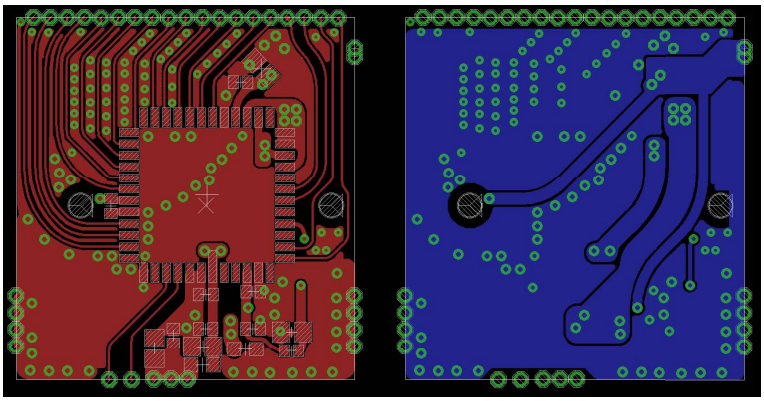

Figure 3.5.6: Drawing of the CMOS image sensor: component side (left) and drawing the other side (right)

3.5.2.3 The main board

Schematic circuit (Fig.3.5.7,3.5.9,3.5.10) optimization includes:

- DC-DC voltage converter replacement to TLV62090 (Texas Instruments). It is step-down voltage converter from 4,2V to 3,3V with efficiency coefficient of 96% at 900mA output current. Maximum output current is 3A.
- Replacing the LCD on NHD-4.3-480272EF-ASXV-CTP (Newhavendisplay). The main improvement is the matrix type MVA (Multi-domain Vertical Alignment), which in turn means wider viewing angle of 150^0 in both horizontal and vertical planes, as well as high contrast. Increased brightness up to $700cd/m^2$. A significant improvement is the capacitive touch panel. Display attached using a 24-bit parallel RGB connection.
- LED current control and management circuit. It is based on high-efficiency step-up voltage converter - MAX1698 (Maxim Integrated). LED intensity adjustment is done in an analogous way, by changing the voltage to the ADJ pin MAX1698. This is achieved with 12-bit I2C interface DAC LTC2631 (Linear Technology). The circuit was added protection against over-voltage output, in case of disconnected light-emitting diode string. This is implemented using the MAX9061 comparators. LED string switching implemented with dual N-type FETs IRLHS6376TRPBFCT (Infineon Technologies).
- Mechanical plug-type connection to the LED ring has been developed.
- Circuit and board added with audible buzzer - MCSMT-8030C-K4082 (MULTICOMP).
- Impulse-type DC-DC converters covered with a metallic shield.
- A variety of improvements for the PCB board have been made.

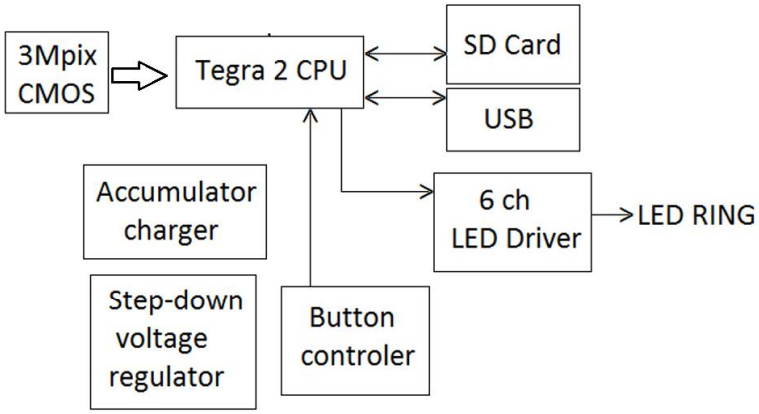

Figure 3.5.7: The block-diagram of SkImager

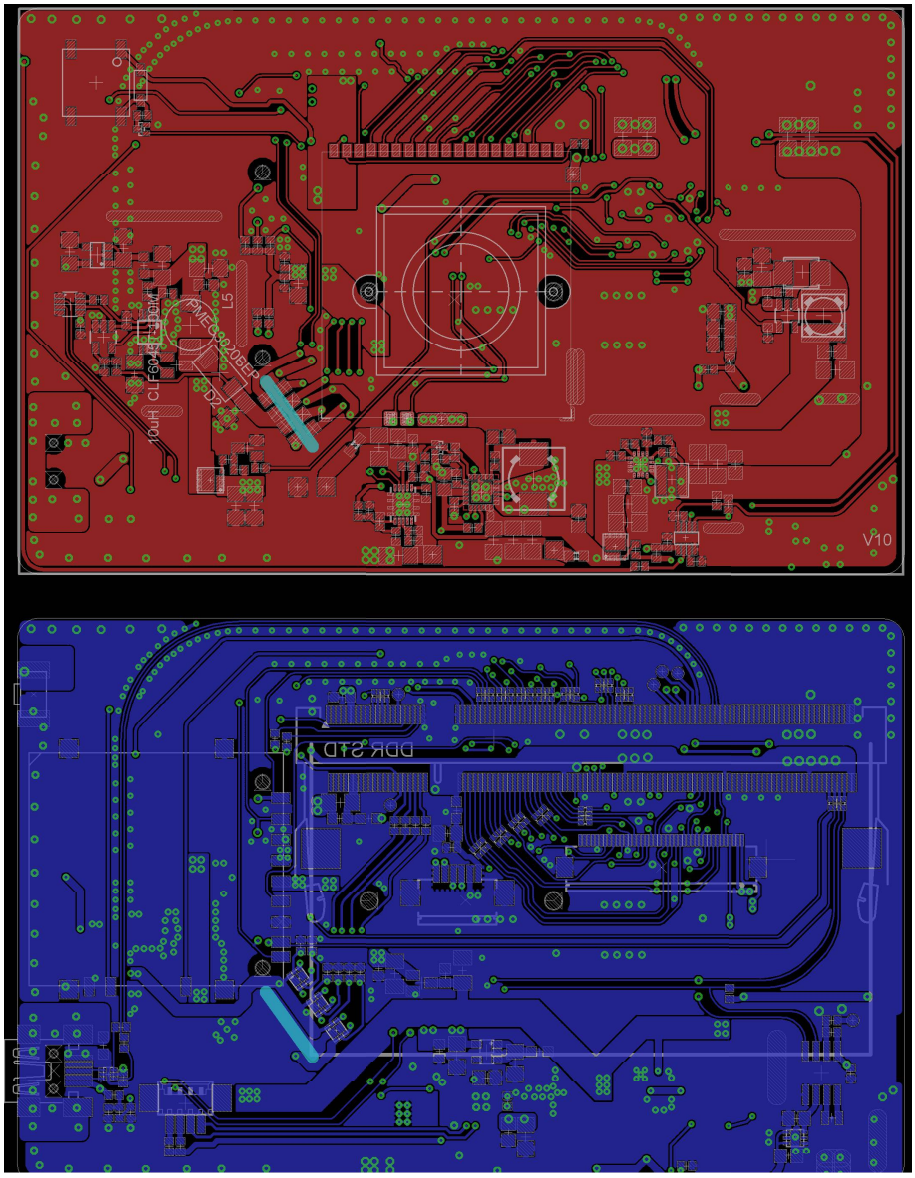

Figure 3.5.8: Main board drawing: component side (left) and drawing the other side (right)

3.5.2.4 Device software improvements

Following tasks were set up for SkImager improvement:

- Make RAW image capture possible.
- Development of look-up table based chromophore mapping mode.
- Development of fluorescence measurement mode.
- Development of microcirculation measurement mode.

- Optimization of software.

Continuing SkImager development RAW image capturing in WEC7 (Windows Embedded Compact 7) operating system was explored and tested. RAW file was successfully captured, file size conforms to resolution and it has RAW format header. Unfortunately pixel data in file is all zeroes. Search for causes of this problem is ongoing.

Camera plugin source code has been updated according to SkImager operating system 1.4 API (Application Programming Interface) changes. New source code definition (header) files were received from COM (Computer On Module) manufacturer Toradex by e-mail. With all the improvements - new source code definition files and plugin source code updates - camera plugin still didn't work completely with operating system version 1.4. Therefore detailed code execution research was done - written down all callback function calls, debug output and other additional parameters. Acquired data was aggregated and sent to COM manufacturer's client support service. At the moment of writing this report a test version alpha1 of next new operating system version 2.0 had just been received from manufacturer with several bug fixes for this problem and testing and search for bugs is ongoing.

Chromophore mapping mode was converted from full-scale every pixel calculation in a device to look-up table based processing. Processing is based on tables where an 8-bit (256 values) chromophore index value is assigned to every one of $224 = 16\ 777\ 216$ RGB color combinations. That way algorithm calculation is effectively transferred to look-up table and that can be generated using complex model calculations in a MATLAB environment on PC (Personal Computer). This kind of approach eases algorithm exploration and development process. Also using look-up table makes chromophore map calculation time independent of algorithm complexity.

Existing SkImager application code does not allow capture mode - still, video or RAW images - dynamic change without software recompilation. Therefore for making RAW image capture, still image based measurement (chromophore mapping, fluorescence) and video based measurement (microcirculation) dynamic mode change possible, a substantial internal architecture of application restructuring has been started. It is mostly related to component using DirectShow multimedia system, user interface and common control of these. This remake is still in development process and it is expected to complete it in a 2nd period of project.

SkImager parallel camera control plugin and control access from user interface application for sensor exposure time adjustment was developed. It makes possible setting exposure time from 1 ms to 44695 ms with granularity of 1 ms.

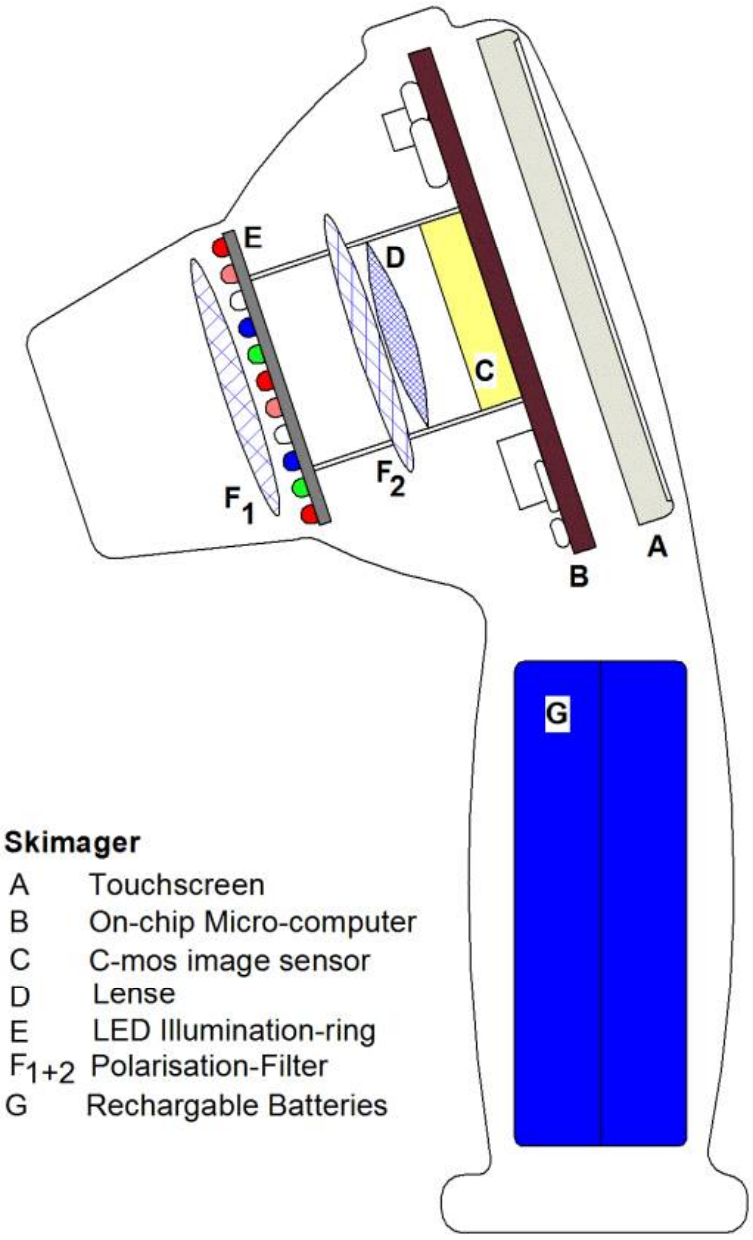

Figure 3.5.9: The prototype device "SkImager"

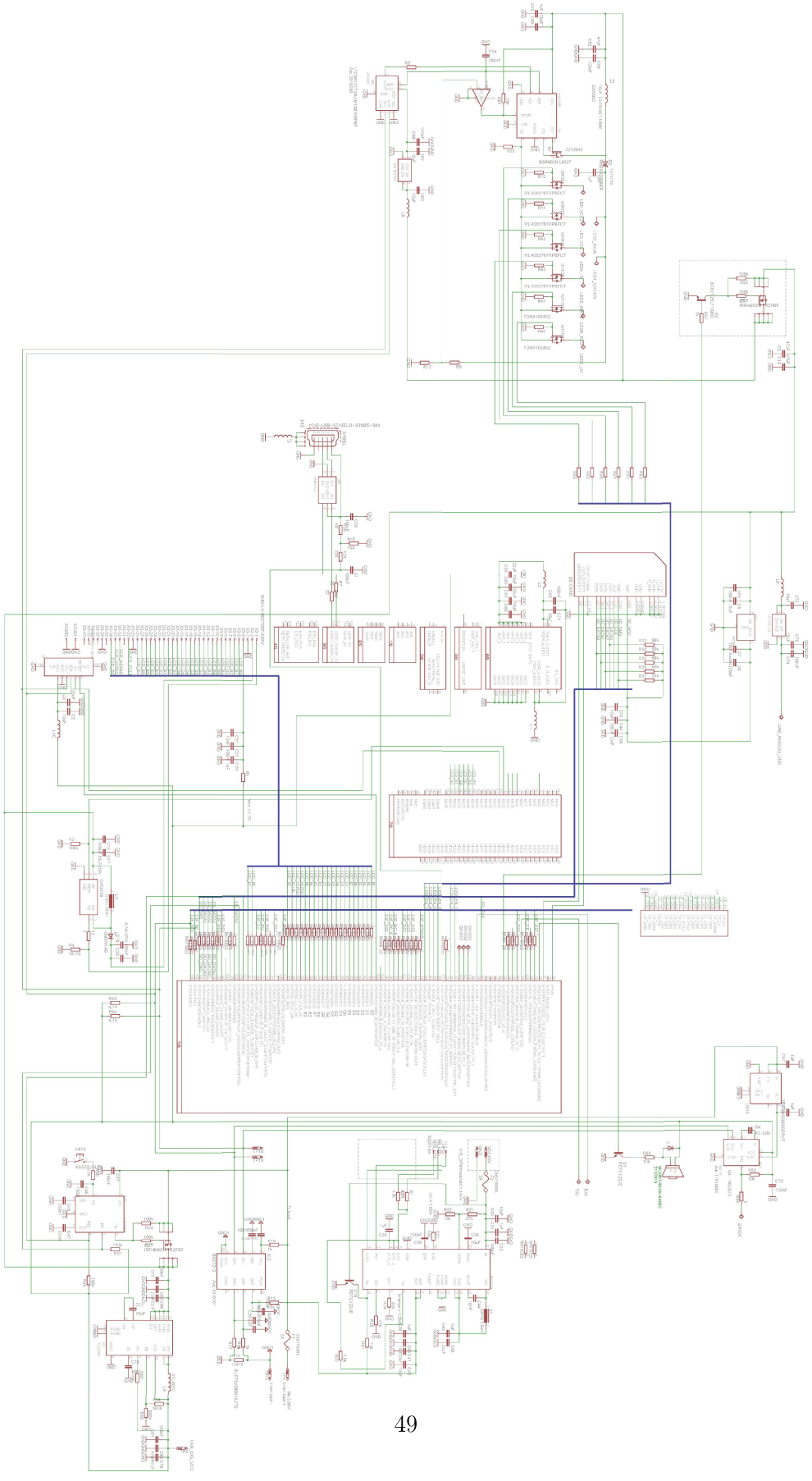

Figure 3.5.10: Schematic diagram of SkImager

Bibliography

[1] J. Spigulis, D. Jakovels, and U. Rubins. Method and device for multispectral imaging by means of a digital rgb sensor, January 5 2012. World Patent: WO2012002787 A1.

[2] J. Spigulis and L. Elste. Method and device for imaging of spectral reflectance at several wavelengths bands, September 19 2013. World Patent: WO2013135311 A1.

[3] J. Spigulis. Method for imaging of spectral reflectance at several wavelengths, January 1 2014. Latvian patent: LV 14782 B.

[4] J. Spigulis, D. Jakovels, and U. Rubins. Rgb imaging system for mapping and monitoring of hemoglobin distribution in skin. In *Proc. of SPIE*, volume 7557, page 75570M, 2010.

[5] J. Spigulis, D. Jakovels, and L. Elste. Towards single snapshot multispectral skin assessment. In *Proc. of SPIE*, volume 8216, page 82160L, 2012.

[6] J. Spigulis and L. Elste. Single snapshot rgb multispectral imaging at fixed wavelengths: proof of concept. In *Proc. of SPIE*, volume 8937, page 89370L, 2014.

[7] D. Jakovels, U. Rubins, and J. Spigulis. Rgb imaging system for mapping and monitoring of hemoglobin distribution in skin. In *Proc. of SPIE*, volume 8158, pages 81580R–1, 2011.

[8] J. Spigulis and I. Oshina. 3x3 technology for snapshot mapping of skin chromophores. In *OSA Technical Digest,doi:10.1364/BODA.2015.JT3A.39*, 2015.

[9] J. Spigulis and I. Oshina. 3x3 technology for snapshot mapping of skin chromophores. In *OSA Optics in the Life Sciences (Vancouver, CA, 12-15/04/2015)*, 2015.

[10] I. Oshina and J. Spigulis. Snapshot mapping of skin chromophores at triple-wavelength illumination. In *Developments in Optics and Communications (Rīga, 10-12/04/2015)*, 2015.

[11] I. Oshina and J. Spigulis. Image processing for snapshot mapping of skin chromophores. In *IONS Karlsruhe 2015 (Karlsruhe, DE, 26-29/06/2015)*, 2015.

[12] J. Spigulis and I. Oshina. Monochomatic spectral imaging: principles and application for skin chromophore mapping. In *The 2nd Israeli Biophotonics Conference (IBPC-2), December 1-2, 2015, Bar-Ilan University, Ramat-Gan, Israel. http://www.ibpc2.org/. Presentation*, 2015.

[13] J. Spigulis, I. Oshina, and Z. Rupenheits. Smartphone single-snapshot mapping of skin chromophores. In *Smartphone single-snapshot mapping of skin chromophores. – OSA Biomed Conference, Fort-Loderdale, 25-28 April 2016 (submitted)*, 2016.

[14] J. Spigulis and I. Oshina. Method and device for chromophore mapping at multiple spectral band illumination, January 1 2015. LV patent application P-15-137.

[15] A. Miščuks, R. Erts, U. Rubīns, J. Spīgulis, and M Mihelsons. Device for the determination of peripheral regional anaesthesia using contactless photoplethysmography, February 02 2012. Latvian patent LV 14444 B.

[16] U. Rubīns, J. Spīgulis, and A. Miščuks. Method and device for monitoring of regional anaesthesia and pain therapy, January 1 2014. Latvian patent LV 14819 B.

[17] U. Rubins, V. Upmalis, O. Rubenis, D. Jakovels, and J. Spigulis. Real-time photoplethysmography imaging system. In *Proc. IFMBE*, volume 34, pages 183–186, 2011.

[18] Spigulis. J. Biophotonic technologies for noninvasive assessment of skin condition and blood microcirculation. *LATV J PHYS*, 49:5, 2012.

[19] U. Rubins, A. Miscuks, O. Rubenis, R. Erts, and A. Grabovskis. The analysis of blood flow changes under local anesthetic input using non-contact technique. In *Proc. BMEI, 2010 3rd Int. Conf.*, volume 2, pages 601–604, 2010.

[20] P. Taroni, I. Bargigia, A. Farina, R. Cubeddu, and A. Pifferi. First in vivo spectral characterization of breast up to 1300 nm. *Proc. SPIE*, 7896:78962L–78962L–4, 2011.

[21] A. N. Bashkatov, E. A. Genina, V. I. Kochubey, and V. V Tuchin. Optical properties of human skin, subcutaneous and mucous tissues in the wavelength range from 400 to 2000 nm. *J. Phys. D. Appl. Phys.*, 38:2543–2555, 2005.

[22] R. H. Wilson, K. P. Nadeau, F. B. Jaworski, B. J. Tromberg, and A. J. Durkin. Review of short-wave infrared spectroscopy and imaging methods for biological tissue characterization. *J. Biomed. Opt.*, 20(3):030901, 2015.

[23] J. W. et al. Fluhr. Comparative study of five instruments measuring stratum corneurn hydration (comeometer cm 820 and cm825, skicon 200, nova dpm 9003, dermalab). *In vitro. Ski. Res. Technol.*, page 161–170, 1999.

[24] Descamps Leveque L. Rigal Bazin, Sturelle. Near infrared spectroscopy: a new approach to the characterisation of dry skin. *Ifscc*, 209:197–209, 1993.

[25] K. Martin. Direct measurement of moisture in skin by nir spectroscopy. *Cosmet. Chem.*, 261:249–261, 1993.

[26] E.-J. Suh, Y.-A. Woo, and H.-J. Kim. Determination of water content in skin by using a ft near infrared spectrometer. *Arch. Pharm. Res.*, 28:458–462, 2005.

[27] H. Iwasaki, K. Miyazawa, and S. Nakauchi. Visualization of the human face skin moisturizing-ability by spectroscopic imaging using two near-infrared bands. 6062:1–8, 2006.

[28] H. Arimoto and M. Egawa. Water content distribution imaging of skin tissue using near-infrared camera and measurement depth analysis. 8587:85871T, 2013.

[29] Oregon Medical Laser Centre. Optical properties spectra, http://omlc.org/spectra/, 2015.

[30] T. Maeda, N. Arakawa, M. Takahashi, and Y. Aizu. Monte carlo simulation of spectral reflectance using a multilayered skin tissue model. *Opt. Rev.*, 17:223–229, 2010.

[31] S. J. Matcher, M. Cope, and D. T. Delpy. In vivo measurements of the wavelength dependence of tissue-scattering coefficients between 760 and 900 nm measured with time-resolved spectroscopy. *Appl. Opt.*, 36:386–396, 1997.

[32] J Spigulis, U. Rubins, E. Kviesis-Kipge, and Rubenis O. Skimager:a concept device for in-vivo skin assessment by multimodal imaging. *Proc.Est.Acad.Sci.*, 63(3):213–220, 2014.

[33] J Spigulis, U. Rubins, and E. Kviesis-Kipge. Multimodal imaging device for non-contact skin diagnostics, January 1 2013. Latvian patent LV 14749 B.